Journal of Sound and Vibration (2001) **240**(2), 263–292
doi:10.1006/jsvi.2000.3231, available online at http://www.idealibrary.com on IDEAL®

PREDICTION OF VIBRATIONAL ENERGY DISTRIBUTION IN THE THIN PLATE AT HIGH-FREQUENCY BANDS BY USING THE RAY TRACING METHOD

K.-S. Chae and J.-G. Ih

Center for Noise and Vibration Control, Department of Mechanical Engineering, Korea Advanced Institute of Science and Technology, Science Town, Taejon 305-701, *Korea.*
E-mail: ihih@sorak.kaist.ac.kr

(*Received* 6 *July* 1999, *and in final form* 20 *June* 2000)

At high frequencies, one is interested in both the energy distribution and the energy flow of connected vibrating structures. The prediction of time- and space-integrated energy quantity has been usually performed by the statistical energy analysis (SEA), whereas the vibration conduction analysis (VCA) was suggested for calculating the time-averaged spatial energy distribution in structures. However, the VCA has not been useful due to inaccuracies in predicting the energy distribution and estimating the vibration transmission through structural joints. In this article, the ray tracing method (RTM) for high-frequency plate flexural vibration is suggested for solving the foregoing problems. The ray tube concept is adopted for describing the emanating circular wave and the governing relationships are derived for incident, reflected, and transmitted ray tubes at the coupled boundaries. The proposed RTM is applied to the prediction of the time-averaged vibration distribution in a single square panel and two line-coupled square plates. In addition, a four-panel array is investigated for the performance of the proposed RTM in analyzing the vibration transmission characteristics by panel joints. The results reveal that an improved prediction of spatial energy distribution can be obtained compared with SEA and VCA. It is also noted that the performance of the RTM is very similar to that of the wave intensity analysis (WIA) although RTM results seems to be slightly better.

1. INTRODUCTION

The calculation efficiency of modal methods will become lower or the calculation itself is often obsolete at the mid- or high-frequency bands in which the involved wavelength is comparatively much smaller than the characteristic size of the structure. Additionally, those methods have limited frequency range for reliable results due to the uncertainties involved in the structure. Statistical energy analysis (SEA) [1] has been used for the high-frequency vibro-acoustic analysis although the results are expressed only by time-averaged and spatially integrated energies.

In order to enable the calculation of the spatial distribution of vibration energy, many works have been done. Nefske and Sung [2] suggested the so-called *power flow analysis* or *energy flow finite element method* by using the vibration conduction equation derived for one-dimensional vibrating structures. Wohlever and Bernhard [3] reexamined the vibration conduction relationship for the rod and beam structures. Bouthier and Bernhard [4–6] showed that the vibration analogy with heat conduction is valid for the

0022-460X/01/070263 + 30 $35.00/0

two-dimensional vibration field composed of plane wave components. However, Langley [7, 8] pointed out that there is a discrepancy between the solution of the vibration conduction analysis (VCA) and the exact solution for the infinite two-dimensional structure. Kim *et al.* [9] suggested a modified vibration conduction equation in the cylindrical co-ordinate and then the far-field energy became the same with the exact value. Langley [8] also showed that the two-dimensional vibration conduction equation would be valid only for the structure having a relatively small damping factor or highly reverberant wave field. If this is true, this method is not much fascinating compared with SEA except the possibility of using any commercial package for solving heat conduction problems in the structural vibration analysis. There will be a little variation distribution in each subsystem due to the high level of reverberations and the resulting vibration field will have noting but a uniform energy distribution that can be handled easily by the SEA.

Carcaterra and Sestieri [10] derived the power balance equation for one- and two-dimensional vibrating structures through some operations on the Navier equation. They also suggested an *envelope energy model* by utilizing the Hilbert transform for flexural beams and showed that this envelope energy model yielded close result to the exact solution near the excitation point and the boundaries [11]. Later, they refined the envelope energy model for the analysis of complex envelope displacement by which spatial fluctuations of the displacement could be predicted [12]. However, this technique looks rather complex to be applicable to the complex structures.

Smith [13] had suggested a hybrid energy method for the single-plate problem in which the total vibration field is divided into a direct field and a reverberant field. By applying this concept to a point-excited single plate, he could obtain the energy distribution over the plate that was very close to the result by exact analysis irrespective of the damping strength. Le Bot [14, 15] also pointed out that the assumption of plane wave field might fail for largely non-diffuse fields and suggested differential equations for each of plane, cylindrical, and spherical wave fields. By using the Huygens principle and the solutions from differential equations for cylindrical and spherical waves, he derived a vibroacoustic model for the two-dimensional structure and the three-dimensional acoustic enclosure. The result for a cavity was very similar to that by the acoustic ray tracing.

One of the limitations of SEA is that the method sometimes yields unreliable prediction of the vibration transmission for coupled structures. In applying SEA technique to two-dimensional structures such as flat plates, the coupling loss factors are generally derived under the diffuse field assumption. However, this diffuse field assumption is far from the reality in many coupled structures. Wave intensity analysis (WIA) technique suggested by Langley [16, 17] is an extension of SEA in which the diffuse field assumption was removed. In this method, the incident wave energy upon structural junction between plates is assumed being variable with respect to the incident angle and the variation of transmission coefficient can be included in the power balance equations between the directional wave energies. Due to these favorable characteristics, WIA can deal with the wave filtering phenomena at the coupled boundaries and can give more enhanced prediction in comparison with the conventional SEA. Contrastingly, in the vibration conduction analysis (VCA) and Smith's hybrid energy method, the directional wave energy has not been considered but the total reverberant energy was considered. Consequently, it is doubtful that the VCA can deal with the wave filtering phenomena for two-dimensional coupled structures or three-dimensional coupled acoustical volumes.

The ray tracing method (RTM) is one of the geometrical acoustics techniques and has been widely applied to the room acoustics areas to predict the acoustic impulse response

and the acoustic field distribution at high frequencies. The impulse response of a room is build up by transient sound signals, which comes from the propagation of acoustic waves with time. Schroeder [18, 19] tested the primitive idea in calculating the impulse response in rooms. Krokstad *et al.* [20] used a mathematical model of a hall, which is excited by a sound pulse emitted from a fixed point source. Energy is carried by rays equally distributed over the whole or over a selected part of the solid angle. The life history of each ray is calculated by assuming geometrical reflection at all surfaces, until the ray strikes the audience area where it is assumed to be totally absorbed. Kulowski [21] reported on an algorithm for the sound ray tracing in a three-dimensional space in the viewpoint of economizing both the calculation time and the computer memory space. However, the characteristics of omni-directional source by a sound pulse cannot be guaranteed by tracing the omni-directionally generated rays represented by lines. Maercke and Martin [22] proposed a "conical beam model" in order to model an omni-directional radiation pattern from a source, in which each ray is modelled as a conical beam shape. Lewer [23] suggested a "triangular beam method" in which each ray is modelled as a triangular beam. The echogram can be obtained by collecting the contributions from all rays on the receiver position.

RTM has been used mainly for the prediction of transient sound pressure levels in rooms by summing the acoustic energy traces for the receiver position. The prediction of steady state response such as frequency response function by using RTM has been a pending question until recently. Vorländer [24] proposed a method for predicting the frequency response function from high-accuracy energy impulse response by using a "combined ray tracing/image-source algorithm". Image-source algorithm is another method of geometrical acoustics that should use the Fourier transform, but has very similar characteristics with RTM.

Recently, several attempts on the frequency response prediction by using the ray tracing concept were carried out. Geest and Patzold [25] used the "phased ray tracing algorithm" in which, when calculating the contributions of the various reflections, a varying phase with a ray propagation was included. They reported a good agreement of the predicted frequency response function with that by boundary element method for an acoustic enclosure with specular reflective walls. Shin and Ih [26] also studied the characteristics of such technique for several geometric acoustic models and confirmed its applicability and limitation in the mid-frequency range above the Schroeder cut-off frequency.

In structural acoustics field, Cremer *et al.* [27] and Skudrzyk [28] has applied the ray tracing concept to the wave summation in the vibrating simple rod. Gunda *et al.* [29] analyzed a simple square plate by using the image source method. Parot and Thirard [30] used RTM to the vibration analysis of a truss structure and a coupled plate. Recently, Hugin [31] has extended the wave summation method of Cremer *et al.* [27] into the vibration analysis of coupled beam structures. They showed that the proposed ray tracing method was valid in the middle- and high-frequency ranges in the vibration of the coupled one-dimensional structure.

In this paper, the ray tracing method for high-frequency structural vibration is studied for the analysis of flexural vibration of flat thin-plate structures. A ray tube model is suggested which satisfies the high-frequency assumptions at the source point and the coupling boundaries. A single square plate and two coupled plates are analyzed by the proposed RTM and the results are compared with those by SEA, VCA and analytical calculation. In order to test the proposed RTM in calculating the vibration transmission characteristics, a four panel array used by Langley [16] is also analyzed and comparisons are made with SEA, VCA, WIA and analytical calculation.

2. RAY TRACING METHOD FOR FLEXURAL VIBRATION OF THIN PLATE

2.1. ENERGY DENSITY AND INTENSITY VECTOR IN A THIN PLATE

The flexural displacement of a thin, transversely vibrating plate excited by time harmonic force $Fe^{j\omega t}$ at a point, oscillating with a circular frequency ω, is governed by

$$D\nabla^4 w(x, y) - \rho h\omega^2 w(x, y) = F\delta(x - x_f, y - y_f), \tag{1}$$

where $w(x, y)$ is the flexural displacement, D is the complex bending stiffness as $D_0(1 + j\eta)$, in which D_0 is the bending stiffness and η is the loss factor, ρ is the material density, h is the plate thickness, F is the magnitude of time harmonic force, and (x_f, y_f) is the excitation position. For stationary time harmonic response, the time-averaged kinetic energy $T(x, y)$ and potential energy density $U(x, y)$ is given by [6].

$$T(x, y; \omega) = (\rho h\omega^2/4)|w|^2, \tag{2}$$

$$U(x, y; \omega) = \frac{D_0}{4}\left(\frac{\partial^2 w}{\partial x^2}\left(\frac{\partial^2 w}{\partial x^2}\right)^* + \frac{\partial^2 w}{\partial y^2}\left(\frac{\partial^2 w}{\partial y^2}\right)^* + 2\mu\frac{\partial^2 w}{\partial x^2}\left(\frac{\partial^2 w}{\partial y^2}\right)^* + 2(1-\mu)\frac{\partial^2 w}{\partial x\partial y}\left(\frac{\partial^2 w}{\partial x\partial y}\right)^*\right). \tag{3}$$

Here, $*$ denotes the complex conjugate and μ is the Poisson ratio. The time-averaged flexural wave intensity in the x and y direction can be expressed as [32]

$$I_x = \frac{\mathrm{Re}}{2}\left[D\left(\left(\frac{\partial^3 w}{\partial x^3} + \frac{\partial^3 w}{\partial x\partial y^2}\right)(j\omega w)^* - \left(\frac{\partial^2 w}{\partial x^2} + \mu\frac{\partial^2 w}{\partial y^2}\right)\left(j\omega\frac{\partial w}{\partial x}\right)^* - (1-\mu)\left(\frac{\partial^2 w}{\partial x\partial y}\right)\left(j\omega\frac{\partial w}{\partial y}\right)^*\right)\right], \tag{4}$$

and

$$I_y = \frac{\mathrm{Re}}{2}\left[D\left(\left(\frac{\partial^3 w}{\partial x^2\partial y} + \frac{\partial^3 w}{\partial y^3}\right)(j\omega w)^* - \left(\mu\frac{\partial^2 w}{\partial x^2} + \frac{\partial^2 w}{\partial y^2}\right)\left(j\omega\frac{\partial w}{\partial y}\right)^* - (1-\mu)\left(\frac{\partial^2 w}{\partial x\partial y}\right)\left(j\omega\frac{\partial w}{\partial x}\right)^*\right)\right]. \tag{5}$$

Because the near-field wave components are acting only at the near excitation points or discontinuities such as supporting boundaries or coupled boundaries, the displacement w at a position which is sufficiently remote from discontinuities or excitations can be approximately expressed with the directional plane waves as follows [8, 33]:

$$w(x, y; \omega) \approx \int_0^{2\pi} \hat{w}(\theta) e^{-jk(x\cos\theta + y\sin\theta)}\, d\theta. \tag{6}$$

For $\eta \ll 1$, the complex wavenumber k is given by

$$k = k_0 - j\alpha/2, \tag{7}$$

where k_0 is the wavenumber in the absence of damping, α is the damping coefficient that is equivalent to $\omega\eta/c_g$, and c_g is the group velocity that is given by $2\sqrt{\omega}\sqrt[4]{D_0/\rho h}$.

If there is only one plane wave along a direction, the displacement can be assumed as $w = \hat{w}e^{-j\mathbf{k}(\cos\theta x + \sin\theta y)}$, the vibration energy density can be derived from equations (2) and (3) as

$$e(x, y; \omega) = T(x, y; \omega) + U(x, y; \omega) = \tfrac{1}{2}\rho h\omega^2 |\hat{w}|^2 \exp[-\alpha(x\cos\theta + y\sin\theta)]. \quad (8)$$

From equations (4) and (5), the vibration intensity distribution by this wave is given by

$$\mathbf{I}(x, y; \omega) = c_g e(x, y; \omega)(\cos\theta \mathbf{i}_x + \sin\theta \mathbf{i}_y), \quad (9)$$

where $\mathbf{i}_x$ and $\mathbf{i}_y$ are unit vectors in the x and y directions respectively.

If there are a number of directional plane waves as in equation (6), the energy density can be obtained by substituting equation (6) into equations (2) and (3). Thus, the kinetic energy can be expressed as

$$T(x, y; \omega) = (\rho h\omega^2/4) \int_0^{2\pi} \int_0^{2\pi} \hat{w}(\theta_1)\hat{w}^*(\theta_2) e^{-j\mathbf{k}(x\cos\theta_1 + y\sin\theta_1)} e^{-j\mathbf{k}^*(x\cos\theta_2 + y\sin\theta_2)} \, d\theta_1 \, d\theta_2. \quad (10)$$

If all wave components were considered to be statistically independent, i.e., a random wave field, the interference between the waves propagating in different directions can be neglected.

Then, approximately equation (10) can be written as

$$T(x, y; \omega) = (\rho h\omega^2/4) \int_0^{2\pi} |\hat{w}(\theta)|^2 e^{-\alpha(x\cos\theta + y\sin\theta)} \, d\theta. \quad (11)$$

Similarly, the potential energy can be approximately written as

$$U(x, y; \omega) = \frac{D|k|^4}{4} \int_0^{2\pi} |\hat{w}(\theta)|^2 e^{-\alpha(x\cos\theta + y\sin\theta)} \, d\theta = T(x, y; \omega). \quad (12)$$

Therefore, the energy density can be approximated as [16]

$$e(x, y; \omega) = 2T(x, y; \omega) = (\rho h\omega^2/2) \int_0^{2\pi} |\hat{w}(\theta)|^2 e^{-\alpha(x\cos\theta + y\sin\theta)} \, d\theta, \quad (13)$$

or it can be derived from the directional integration of wave energy $e(x, y; \omega, \theta)$ as follows [16]:

$$e(x, y; \omega) = \int_0^{2\pi} e(x, y; \omega, \theta) \, d\theta. \quad (14)$$

In the vibration field at high frequencies, the wavelength becomes considerably smaller than the characteristic size of the structure. There will be a number of vibration modes and the strong modal overlap between them, that the exact vibration displacement or phase distributions are losing their importance. In the viewpoint of vibration intensity, the local vortex phenomenon due to the vibration modes becomes less important. On the contrary, the approximated energies and the overall power flow paths are more important in analyzing the vibration and the associated noise problem. Therefore, the frequency band analysis in terms of the vibration energy and intensity is the most appropriate method in the high-frequency range. The band-integrated kinetic energy can be written as

$$T_b(x, y) = \int_{\omega_1}^{\omega_2} (\rho h\omega^2/4) \left(\int_0^{2\pi} \int_0^{2\pi} \hat{w}(\omega, \theta)\hat{w}^*(\omega, \vartheta) e^{-j\mathbf{k}(x\cos\theta + y\sin\theta)} e^{-j\mathbf{k}^*(x\cos\vartheta + y\sin\vartheta)} \, d\theta \, d\vartheta \right) d\omega, \quad (15)$$

where ω_1 and ω_2 are the lower and upper band limit respectively. Because the interference components between the different directional plane waves have fluctuating characteristics with the frequency variation, these components would be smeared out by the band integration. Then, if the band width $\Delta\omega_c$ $(=\omega_2 - \omega_1)$ is comparatively smaller than the center frequency ω_c,

$$T_b(x, y) \approx (\rho h \omega_c^2/4)\left(\int_0^{2\pi} |\hat{w}(\omega_c, \theta)|^2 \, \mathrm{e}^{-\alpha(x\cos\theta + y\sin\theta)} \, \mathrm{d}\theta\right)\Delta\omega_c. \tag{16}$$

The same procedure can be applied to the band-integrated potential energy $U_b(x, y)$ and the band-integrated energy density can be approximately given by

$$\begin{aligned} e_b(x, y) &= T_b(x, y) + U_b(x, y) \approx 2T_b(x, y) \\ &= (\rho h \omega_c^2/2)\left(\int_0^{2\pi} |\hat{w}(\omega_c, \theta)|^2 \mathrm{e}^{-\alpha(x\cos\theta + y\sin\theta)} \, \mathrm{d}\theta\right) \Delta\omega_c \end{aligned} \tag{17}$$

or

$$e_b(x, y) = \Delta\omega_c \int_0^{2\pi} \mathrm{e}(x, y; \omega_c, \theta) \, \mathrm{d}\theta. \tag{18}$$

Equation (17) or equation (18) is derived only with the assumption that interference terms are to be cancelled out by the band-integration process. Equation (18) can also be directly derived from equation (14) with the band-integration. The neglect of the interferences between directional waves can be justified when the directional waves are incoherent or of frequency-averaging process.

The band-integrated energy density $e_b(x, y)$ is the result of the superposition of the directional energy densities $e_b(x, y; \theta)$ in which θ is the propagation direction:

$$e_b(x, y) = \int_0^{2\pi} \mathrm{e}_b(x, y; \theta) \, \mathrm{d}\theta. \tag{19}$$

In SEA in which the diffusive wave field is assumed, the directional wave energy density is simply given by

$$e_b(x, y; \theta) = \frac{e_b(x, y)}{2\pi} = \frac{\langle e_b \rangle}{2\pi S}, \tag{20}$$

where S is the area of the two-dimensional vibration field and the symbol $\langle\ \rangle$ represents the spatial integration. That is, SEA cannot deal with the directional wave energy and spatial variation of energy density. The directional wave energy in WIA is assumed non-uniform with respect to the heading direction of the wave and uniform over the space. In this case, $e_b(x, y; \theta)$ can be represented as

$$e_b(x, y; \theta) \equiv \frac{\langle e_b(\theta) \rangle}{S}. \tag{21}$$

Here, $\langle e_b(\theta) \rangle$ is the space-integrated directional energy at each position that is denoted as $E(\theta)$ in WIA [16]. This reveals that WIA cannot deal with the spatial distribution of energy density, although WIA can deal with the directional wave energy.

Through the same procedure applied on the band-integrated energy density, the band-integrated vibration intensity vector $\mathbf{I}_b(x, y)$ at a position can be approximately written as

$$\mathbf{I}_b(x, y) = \int_0^{2\pi} c_g e_b(x, y; \theta)(\mathbf{i}_x \cos\theta + \mathbf{i}_y \sin\theta)\,\mathrm{d}\theta. \tag{22}$$

The foregoing summarized expressions for energy density and intensity vector will be applied in the development of RTM in the next section.

2.2. BASICS OF RTM

The frequency response function $H(\mathbf{x}, \mathbf{x}_f; \omega)$ under the steady state excitation could be resolved by the Fourier transform of the impulse response as follows:

$$H(\mathbf{x}, \mathbf{x}_f; \omega) = \int_{-\infty}^{\infty} h(\mathbf{x}, \mathbf{x}_f; t)\,\mathrm{e}^{-\mathrm{j}\omega t}\,\mathrm{d}t. \tag{23}$$

Here, $\mathbf{x}$ and $\mathbf{x}_f$ mean the observation point (x, y) and the excitation position (x_f, y_f) respectively. The initial stage of impulse response is like that in the infinite structural element, $h_\infty(\mathbf{x}, \mathbf{x}_f; t)$, and the subsequent signals can be defined as the impulse response of reflected wave field, $h_{ref}(\mathbf{x}, \mathbf{x}_f; t)$, that is,

$$h(\mathbf{x}, \mathbf{x}_f; t) = h_\infty(\mathbf{x}, \mathbf{x}_f; t) + h_{ref}(\mathbf{x}, \mathbf{x}_f; t). \tag{24}$$

When the structural connections exist between the different structural elements, the transmitted signal can be regarded as a kind of reflected signals. The impulse response function $h_\infty(\mathbf{x}, \mathbf{x}_f; t)$ of an infinite structural element is related to the steady state response of an infinite structural element, $H_\infty(\mathbf{x}, \mathbf{x}_f; \omega)$, as follows:

$$h_\infty(\mathbf{x}, \mathbf{x}_f; t) = \frac{1}{2\pi} \int_{-\infty}^{\infty} H_\infty(\mathbf{x}, \mathbf{x}_f; \bar{\omega})\,\mathrm{e}^{\mathrm{j}\bar{\omega}t}\,\mathrm{d}\bar{\omega}. \tag{25}$$

Substituting equation (25) into equation (23) results in

$$H(\mathbf{x}, \mathbf{x}_f; \omega) = H_\infty(\mathbf{x}, \mathbf{x}_f; \omega) + \int_{-\infty}^{\infty} h_{ref}(\mathbf{x}, \mathbf{x}_f; t)\,\mathrm{e}^{-\mathrm{j}\omega t}\,\mathrm{d}t. \tag{26}$$

The first term represents the direct field and the second term represents the reflected field, which means that the total field is the summation of the direct field, $w_{dir}(\mathbf{x}, \mathbf{x}_f; \omega)$, and the reflected field, $w_{ref}(\mathbf{x}, \mathbf{x}_f; \omega)$, as

$$w(\mathbf{x}, \mathbf{x}_f; \omega) = w_{dir}(\mathbf{x}, \mathbf{x}_f; \omega) + w_{ref}(\mathbf{x}, \mathbf{x}_f; \omega), \tag{27}$$

where

$$w_{dir}(\mathbf{x}, \mathbf{x}_f; \omega) = H_\infty(\mathbf{x}, \mathbf{x}_f; \omega)F(\omega), \quad w_{ref}(\mathbf{x}, \mathbf{x}_f; \omega) = F(\omega)\int_{-\infty}^{\infty} h_{ref}(\mathbf{x}, \mathbf{x}_f; t)\mathrm{e}^{-\mathrm{j}\omega t}\,\mathrm{d}t. \tag{28, 29}$$

Therefore, the vibration field in the frequency domain can be expressed with the free space Green function, $H_\infty(\mathbf{x}, \mathbf{x}_f; \omega)$, and its reflections from the boundaries. If the involved

waves have propagating wave characteristics, the impulse response functions would be build up by $h_\infty(\mathbf{x}, \mathbf{x}_f; t)$ and its successive reflections as follows:

$$h(\mathbf{x}, \mathbf{x}_f; t) = h_\infty(\mathbf{x}, \mathbf{x}_f; t) + \int_{\partial\Omega} h_{ref,1}(\mathbf{x}, \mathbf{x}_{\partial\Omega}; t)\, \mathrm{d}x_{\partial\Omega} + \int_{\partial\Omega} h_{ref,2}(\mathbf{x}, \mathbf{x}_{\partial\Omega}; t)\, \mathrm{d}x_{\partial\Omega} + \cdots . \quad (30)$$

Here, $\partial\Omega$ denotes the boundary, $h_{ref,1}(\mathbf{x}, \mathbf{x}_{\partial\Omega}; t)$ is the first reflection, and $h_{ref,2}(\mathbf{x}, \mathbf{x}_{\partial\Omega}; t)$ is the second reflection, and so on. In the viewpoint of the spectral response, equation (30) can be converted into

$$w(\mathbf{x}, \mathbf{x}_f; \omega) = w_{dir}(\mathbf{x}, \mathbf{x}_f; \omega) + \sum_{n=1}^{\infty} w_{ref,n}(\mathbf{x}, \mathbf{x}_f; \omega), \quad (31)$$

where $w_{ref,n}(\mathbf{x}, \mathbf{x}_f; \omega)$ denotes the wave field formed from the nth reflection. Equation (31) is equivalent to the wave train theory discussed by Cremer *et al.* [27] or Hugin [31].

The quadratic spectral displacement response can be obtained from equation (31) as

$$\begin{aligned} |w(\mathbf{x}, \mathbf{x}_f; \omega)|^2 = {} & |w_{dir}(\mathbf{x}, \mathbf{x}_f; \omega)|^2 + \sum_{n=1}^{\infty} |w_{ref,n}(\mathbf{x}, \mathbf{x}_f; \omega)|^2 \\ & + 2\,\mathrm{Re}(w_{dir}(\mathbf{x}, \mathbf{x}_f; \omega) \sum_{n=1}^{\infty} w^*_{ref,n}(\mathbf{x}, \mathbf{x}_f; \omega)) \\ & + 2\,\mathrm{Re}\left(\sum_{n=1}^{\infty} \sum_{m=1,\, m\neq n}^{\infty} w_{ref,n}(\mathbf{x}, \mathbf{x}_f; \omega) w^*_{ref,m}(\mathbf{x}, \mathbf{x}_f; \omega) \right). \end{aligned} \quad (32)$$

The last two terms on the right-hand side of equation (32) mean the interferences between the direct field and the nth reflected field or interferences between the nth and the mth reflected field. Although the reflected waves actually originate from direct wave, they have phases which differ from each other in general. By applying band integration on equation (32) and by assuming the presence of multiple modes within each band, the response fluctuation due to the interference terms could be flattened out:

$$\int_{\omega_1}^{\omega_2} |w(\mathbf{x}, \mathbf{x}_f; \omega)|^2\, \mathrm{d}\omega \approx \int_{\omega_1}^{\omega_2} \left(|w_{dir}(\mathbf{x}, \mathbf{x}_f; \omega)|^2 + \sum_{n=1}^{\infty} |w_{ref,n}(\mathbf{x}, \mathbf{x}_f; \omega)|^2 \right) \mathrm{d}\omega. \quad (33)$$

Because every trace on the right-hand side of equation (33) at the observation position $\mathbf{x}$ means the freely propagating plane waves, the band-integrated energy density can be approximately obtained from equation (17) as

$$e_b(\mathbf{x}, \mathbf{x}_f) \approx \frac{\rho h \omega^2}{2} \Delta\omega_c \left(|w_{dir}(\mathbf{x}, \mathbf{x}_f; \omega_c)|^2 + \sum_{n=1}^{\infty} |w_{ref,n}(\mathbf{x}, \mathbf{x}_f; \omega_c)|^2 \right) \quad (34)$$

or

$$e_b(\mathbf{x}, \mathbf{x}_f) \approx \Delta\omega_c \left(e_{dir}(\mathbf{x}, \mathbf{x}_f; \omega_c) + \sum_{n=1}^{\infty} e_{ref,n}(\mathbf{x}, \mathbf{x}_f; \omega_c) \right), \quad (35)$$

where $e_{dir}(\mathbf{x}, \mathbf{x}_f; \omega)$ and $e_{ref,n}(\mathbf{x}, \mathbf{x}_f; \omega)$ denote the energy densities contributed by the direct field and the nth reflected field respectively.

If a number of point excitations drive the system, equation (32) can be expanded as

$$w(\mathbf{x}, \mathbf{x}_f; \omega) = \sum_{p=1}^{P} \left\{ w_{dir}(\mathbf{x}, \mathbf{x}_{f,p}; \omega) + \sum_{n=1}^{\infty} w_{ref,n}(\mathbf{x}, \mathbf{x}_{f,p}; \omega) \right\}, \tag{36}$$

where p denotes the index of each point excitation. If the excitations are incoherent from each other and the band integration is performed, the following equation is valid for the multi-excitation condition:

$$e_b(\mathbf{x}, \mathbf{x}_f) \approx \Delta\omega_c \sum_{p=1}^{P} \left(e_{dir}(\mathbf{x}, \mathbf{x}_{f,p}; \omega_c) + \sum_{n=1}^{\infty} e_{ref,n}(\mathbf{x}, \mathbf{x}_{f,p}; \omega_c) \right). \tag{37}$$

2.3. IMPLEMENTATION OF RTM FOR FLEXURAL VIBRATION OF THIN PLATES

2.3.1. *Basic strategy of cylindrical wave tube tracing*

The application of wave train theory to the analysis of the two-dimensional wave field could be thought of just like for the one-dimensional case [27, 28, 31]. However, due to the mathematical complexity in describing the initial and reflected two-dimensional waves, it is quite difficult to calculate exactly the reflected wave field [29, 34, 35]. However, a numerical calculation of the reflected wave field would be possible that would yield acceptable predictions at high frequencies although the exact value could not be obtained.

The direct bending wave field for a point-excited thin plate can be expressed by the wave propagation in an infinite plate [27] and the following approximate displacement response $\hat{w}_{dir}(r)$ can be derived for $|kr| \gg 1$:

$$\hat{w}_{dir}(r) \approx \frac{F}{\mathrm{j}8Dk^2} \sqrt{\frac{2}{\pi kr}}\, \mathrm{e}^{-\mathrm{j}(kr - \pi/4)}. \tag{38}$$

Here, k is the bending wavenumber in the plate and r is the distance between the excitation and observation point, i.e., $r = \sqrt{(x - x_f)^2 + (y - y_f)^2}$. The asymptotic solution in equation (38) has a circularly diverging characteristic centered at the excitation point and is invalid near the excitation point. In order to obtain the finite maximum value of $\hat{w}_{dir}(r)$, one can introduce the initial radius r_0 at which $|\hat{w}_{dir}(r_0)| = |w_{dir}(0)|$. Using the Taylor series expansion, the expression for initial radius r_0 is given by

$$r_0^{-1} \approx \frac{\pi|k|}{2} + \alpha. \tag{39}$$

Equation (39) is identical to the initial radius formula proposed by Smith [13]. For undamped case, $kr_0 = \pi/2 = 0{\cdot}6366$ and, the greater the damping factor, the smaller kr_0 becomes. One can find that $w_{dir}(r)$ approximates to $w_{dir}(0)$ inside r_0 and $\hat{w}_{dir}(r)$ outside r_0.

The approximate solution $\hat{w}_{dir}(r)$ implies a circularly propagating wave from the source position. By discretizing this circular wave into many circularly spreading wave tubes as depicted in Figure 1, one can calculate the direct wave field approximately. If the whole angle of 2π is divided into a number of discrete angle region, the response inside the ray tube area can be estimated for each ray tube. Diffraction, scattering and refraction as well as the specular reflection influence the reflected wave field generated from the incident plane wave. If the boundaries are shaped in straight lines and the reflective condition is assumed to be homogeneous along the lines, the reflected field can be approximately calculated only by the

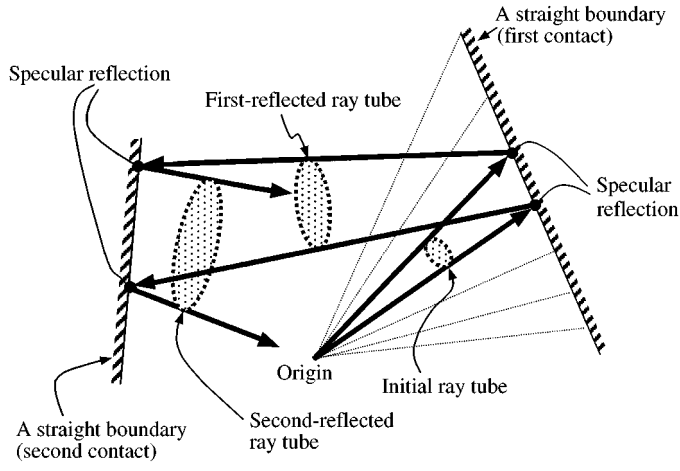

Figure 1. A bundle of ray tubes which is discretized from a circulatory propagating wave. The solid line represents the propagation of a ray tube in the structural wave field confined between two straight boundaries.

specularly reflected ray tubes. The investigation by Gunda *et al.* [29, 34, 35] showed that the diffraction affects only the area near the boundaries in plate vibration.

2.3.2. *Calculation of direct field*

As discussed in the previous section, the vibration field of a thin plate is composed of direct and reflected wave field. Energy response can be also approximately calculated by two energy fields as follows:

$$e(\mathbf{x}) = e_{dir}(\mathbf{x}) + e_{ref}(\mathbf{x}). \tag{40}$$

Here, $e_{dir}(\mathbf{x})$ ad $e_{ref}(\mathbf{x})$ represent direct energy field and reflected energy field, respectively, and the direct energy component can be evaluated from the direct wave field as

$$e_{dir}(\mathbf{x}) = \frac{\rho h |\mathrm{j}\omega \cdot w_{dir}(\mathbf{x})|^2}{2}. \tag{41}$$

Direct energy density distribution can be further simplified as follows:

$$e_{dir}(\mathbf{x}) = \frac{\rho h}{2} \frac{|F|^2}{|Z_\infty|^2} \equiv e_0 \quad \text{for } r \leqslant r_0, \tag{42}$$

$$e_{dir}(\mathbf{x}) = \frac{\rho h}{2} \frac{|F|^2}{|Z_\infty|^2} \frac{r_0}{r} \mathrm{e}^{-\alpha(r-r_0)} = \frac{e_0 r_0}{r} e^{-\alpha(r-r_0)} \quad \text{for } r > r_0. \tag{43}$$

Here, e_0 is defined as the initial energy density at the initial radius r_0 and $Z_\infty (= 8\sqrt{D\rho h})$ is the driving point impedance of an infinite plate.

Direct energy density can also be estimated by using the relation between the observation points and each of the discretized circular ray tubes. Consider a number of ray tubes as shown in Figure 2, which emanated from the source position with an infinitesimal angle $\Delta\theta$. If the receiver point is within the ray tube, the energy density and intensity can be

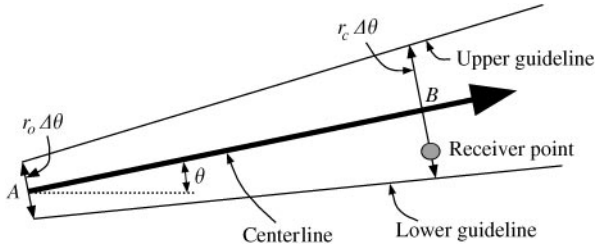

Figure 2. A ray tube model starting with an infinitesimally small angle $\Delta\theta$. The points A and B are positioned within ray tube sections at r_0 and r_c from the origin respectively.

approximately determined by the value at the centerline of the ray tube as follows:

$$e_{dir}(\mathbf{x}) \approx \frac{e_0 r_0}{r_c}\,\mathrm{e}^{-\alpha(r_c - r_0)}, \tag{44}$$

$$I_{dir}(\mathbf{x}) \approx \frac{c_g\, e_0 r_0}{r_c}\,\mathrm{e}^{-\alpha(r_c - r_0)}(\cos\theta\,\mathbf{i}_x + \sin\theta\,\mathbf{i}_y). \tag{45}$$

Here, r_c is the distance of the wave front center from the origin. The foregoing estimation scheme will hold, provided that the distance between the receiver point and the centerline of ray tube, where r_c is estimated, is shorter than the wavelength λ, i.e., $r\Delta\theta/2 \ll \lambda$.

2.3.3. *Calculation of reflected field*

When a ray tube is incident on a boundary, it is equivalent with a plane wave incidence if the width of the incident ray tube is narrow enough compared to the wavelength, i.e., $r\Delta\theta \ll \lambda$. Figure 3 shows a plane wave that is incident on a joint between two coupled plates with an incident angle ϕ_i and being reflected and transmitted. The transmission angle ϕ_j is determined by the Snell's law of $\sin\phi_i/c_i = \sin\phi_j/c_j$, where c_i and c_j denote the phase speed of the vibration were at each plate. Because the guidelines of a ray tube are incident on the boundary and transmitted according to the Snell's law, there is a definite relation between the incident and transmitted ray tubes in their width angles $\Delta\theta_i$ and $\Delta\theta_j$. The latter can be obtained from the difference between two transmission angles of guidelines. Namely, the transmission angle $\phi_{j,h}$ of the upper guideline is determined from $\sin(\phi_i + (\Delta\theta_i/2))/c_i = \sin(\phi_{j,h})/c_j$ and the transmission angle $\phi_{j,l}$ of the lower guideline is determined from $\sin(\phi_i - (\Delta\theta_i/2))/c_i = \sin(\phi_{j,l})/c_j$: finally, one can get $\Delta\theta_j = \phi_{j,h} - \phi_{j,l}$. As depicted in Figure 3, the position of the origin of ray tube is changed due to the transmitted guidelines. The propagation distance r_i of the incident ray tube will be changed to a new propagation distance r_j, where they should follow the geometrical relation $r_i\Delta\theta_i\cos\phi_j = r_j\Delta\theta_j\cos\phi_i$. The power transmission coefficient $\tau_{ij}(\phi_i)$ at the coupled boundary is defined as the ratio between the transmitted power and the incident power normal to the coupled boundary line [27]. Applying this coefficient to the relation between the carrying powers of the incident and the transmitted ray tube, the following relation has to be satisfied between the incident ray tube and the transmitted ray tube:

$$\tau_{ij}(\phi_i)\, c_{g,i} e_i^i L\cos\phi_i \approx c_{g,j} e_j^t L\cos\phi_j. \tag{46}$$

Here, $c_{g,i}$ and $c_{g,j}$ denote the group speed of the vibration wave at each plate respectively. Therefore, the vibration energy density of the transmitted and reflected ray tubes at the

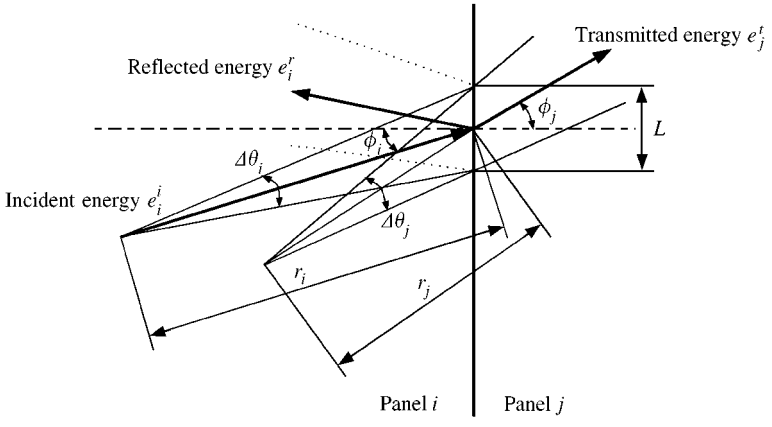

Figure 3. Geometrical schematic and notations of rays involved at the coupled boundary.

coupling boundary can be written as

$$e_j^t = \tau_{ij}(\phi_i)\,(c_{g,i}/c_{g,j})(\cos\phi_i/\cos\phi_j)\,e_i^i \quad \text{and} \quad e_i^r = (1 - \tau_{ij}(\phi_i))\,e_i^i \tag{47}$$

respectively. For a newly generated reflected or transmitted energy tube, the contribution by this ray tube on energy density and intensity at an observation point within the ray tube area can be evaluated as

$$\Delta e_{ref}(\mathbf{x}) \approx \frac{e_1 r_1}{r_c}\,\mathrm{e}^{-\alpha(r_c - r_1)}, \tag{48}$$

$$\Delta I_{ref}(\mathbf{x}) \approx \frac{c_g e_1 r_1}{r_c}\,\mathrm{e}^{-\alpha(r_c - r_1)}(\cos\theta\mathbf{i}_x + \sin\theta\mathbf{i}_y), \tag{49}$$

where e_1 and r_1 are the energy density and the propagation distance, respectively, of the ray tube at the starting boundary position as shown in Figure 4. The final energy density and intensity distribution is the summation of the direct and the reflected energy densities, and intensities respectively. In the foregoing derivations, the transmitted energy field in the connected plate was considered as the reflected energy field.

2.3.4. *Calculation of space-integrated energy*

If energies are calculated at a number of receiver points, the vibration energy distribution can be calculated. In order to obtain the total vibration energy of the plate, the energy traces at the receiver points should be summed. However, this routine requires a long computation time, because the energies at all receiver points within the ray tube should be estimated for every ray tube propagation from a boundary to another. When a ray tube propagates from a boundary to another, its contribution to the total energy of the plate can be simplified as depicted in Figure 4. The amount of contribution by a ray tube to the total energy $\langle e\rangle_i$ of the ith plate is given by

$$\Delta\langle e\rangle_i \approx \int_{r_1}^{r_2} \mathrm{e}(r)\Delta\theta r\,\mathrm{d}r = \mathrm{e}(r_1)r_1\Delta\theta(1 - \mathrm{e}^{-\alpha(r_2 - r_1)})/\alpha, \tag{50}$$

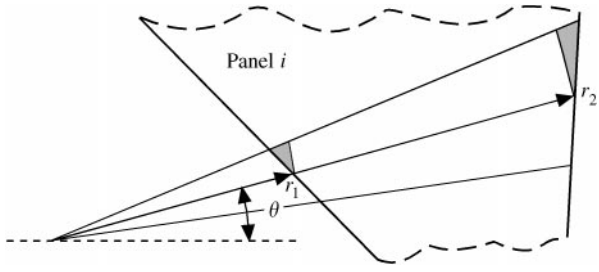

Figure 4. A ray tube propagating from a panel boundary to another.

where r_1 is the propagated distance of the ray tube at the starting boundary from the origin and r_2 at the newly encountered boundary. The band-integrated energy $\langle e_b \rangle_i$ can be approximately written as $\langle e_b \rangle_i = \Delta\omega_c \langle e(\omega_c) \rangle_i$. Similarly, the contribution by this ray tube to the total directional wave energy $\langle e(\theta) \rangle_i$ of the ith plate can be determined for the range of $(\theta_0 - \Delta\theta/2) < \theta < (\theta_0 + \Delta\theta/2)$ as

$$\Delta \langle e(\theta) \rangle_i \approx \Delta \langle e \rangle_i / \Delta\theta. \tag{51}$$

2.3.5. *Convergence condition*

The convergence of RTM prediction should be viewed with respect to the area-integrated value of the energy density response and the minimum propagation distance for convergence. For a point excited single plate with fully reflective boundary conditions, the space-integrated vibration response can be approximately calculated for the propagated distance r as follows:

$$\langle e \rangle \approx e_0 \pi r_0^2 + \int_{r_0}^{r} e(r)\, 2\pi r \, \mathrm{d}r = e_0 \pi r_0^2 + e_0 r_0 2\pi (1 - \mathrm{e}^{-\alpha(r - r_0)})/\alpha. \tag{52}$$

Therefore, in a reverberant condition, the spatially integrated quadratic value reaches 99% of the final result when $\mathrm{e}^{-\alpha(r - r_0)} = 0{\cdot}01$. Therefore, in the single-plate problem, one can obtain a 99% converged prediction with the propagated distance r_{lim} is limited to

$$r_{lim} = -\log_e (0{\cdot}01)/\alpha. \tag{53}$$

When a plate is under the non-reverberant condition, i.e., if the direct field is very strong compared to the reflected field, the limiting propagation distance have to be longer than at least the typical size of the plate in question.

When $n \ll 1$ and propagated radius r goes to infinity, r_0^{-1} is nearly equal to $\pi k/2$ and equation (53) becomes

$$\langle e \rangle \approx e_0 \pi r_0^2 + \int_{r_0}^{\infty} e(r)\, 2\pi r \, \mathrm{d}r = \frac{|F|^2}{4\pi\omega |Z_\infty|} + \frac{|F|^2}{2\omega\eta |Z_\infty|} \approx \frac{|F|^2}{2\omega\eta |Z_\infty|}, \tag{54}$$

which is the same form with the usual SEA result for a single plate.

2.4. CHARACTERISTICS OF RTM

2.4.1. *Computation efficiency of RTM*

A very long calculation time is required for using the ray tracing method in the following involved computations: first, the generation of ray tubes is needed and, second, the

propagation, reflection, transmission of each ray tube should be calculated. Finally, the generated ray tubes should be stored for each structure and later fetched again in order to continue the computation for the propagation of each tube in structures. In addition, a number of ray tubes should be employed for ensuring the calculation for the convergence. For a single plate, the computational efficiency of RTM can be described by r_{lim}. Because $r_{lim} \propto 1/\eta\sqrt{\omega}$, in fact, computation time becomes longer with small η and low ω values. In order to ensure the width of the ray tube to be smaller than the wavelength until the end of calculation for convergence, the condition of $\Delta\theta \ll \lambda/r_{lim}$ has to be imposed on and the initial angle division should be carried out under this condition.

The wave intensity analysis (WIA) method assumes that the plane wave for each direction can be expanded into Fourier series of circular functions. These series will be substituted into the power balance equation for the directional plane waves and the Galerkin procedure is required to get the coefficients of the circular functions. Somewhat complicated integration is involved during this process and a number of Fourier functions are needed for improving the convergence of calculated result [16]. Whenever the analyzed structure is changed, every time in using WIA, one should carry out a new integration at line boundaries, whereas the RTM requires only simple data because the calculation routine is prepared already. In terms of the calculation time, SEA offers the fastest estimation of the structural behavior in vibration. Therefore, it is thought that the computational efficiency should not be evaluated only by the required time.

2.4.2. *Comparison of RTM with other high-frequency methods*

When all the wave actions in the structure are known well, one can obtain the energy and intensity distribution over the whole structure, in principle. However, WIA, SEA and VCA are based upon the simplified energy models such as the power balance equation or the vibration conduction equation. SEA is on the grounds of the reverberant diffuse field, WIA is based on the reverberant field built up by the uncorrelated, independently behaving directional waves, the VCA assumes the wave field made up of plane waves. In contrast, the suggested RTM is based upon the approximately evaluated wave field within the structure by tracing the circular wave tubes. The suggested RTM is not based on the simplified energy model but tries to find out all the effective wave motions within the plate. If the assumed conditions are fulfilled and the assumed behavior of each ray tube is in good accuracy, predictions by RTM would be close to the real things happening in the plate. Because of their theoretical foundation, SEA and VCA cannot deal with the directional wave energy and WIA cannot yield spatial distribution of energy field, but RTM is able to deal with the directional wave energy and can yield the spatial distribution of dynamic properties. Although VCA can calculate the spatial distribution of energy density, VCA, that is based on the plane wave assumption, cannot exactly describe the direct field formed by circularly diverging waves; however, the suggested RTM can take into account the direct field very precisely. Additionally, owing to the fact that RTM can deal with the directional wave information, the result is expected to include the wave filtering effect [16] across the structural line junctions of the plate, whereas SEA and VCA results cannot include this effect because they are based on the angle-averaged transmission coefficients [16].

3. APPLICATION TO THIN PLATES

3.1. SINGLE PLATE

A square plate with an edge length of 2 m is excited at the center with a normal point force of 1 N. All edges are simply supported. Material properties of the steel plate are

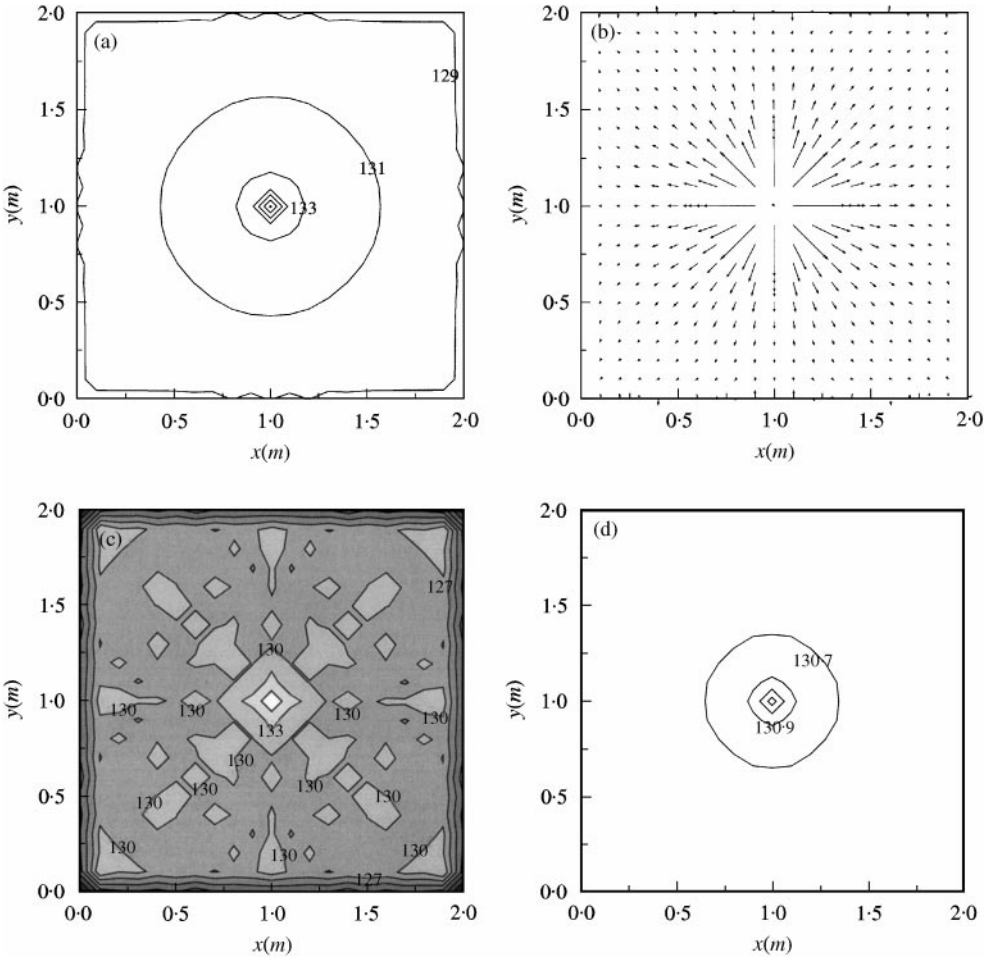

Figure 5. Predicted results for a single panel excited at the center point ($\eta = 0{\cdot}01, f_c = 1$ kHz in $\frac{1}{3}$-octave band). (a), (c), (d) Predicted distribution of vibration levels (dB re 1e-8 m/s); (b) intensity vectors. (a), (b) RTM; (c) mode summation method; (d) VCA. SEA result for this case is 130·6 dB.

specified as follows and the same physical and geometrical data will be used throughout this paper except the case specified otherwise: density $\rho = 7800\ \text{kg/m}^3$; Young's modulus $Y = 2 \times 10^{11}\ \text{N/m}^2$; Poisson ratio $\mu = 0{\cdot}3$; loss factor is either $\eta = 0{\cdot}01$ or $0{\cdot}1$; thickness $h = 1{\cdot}5$ mm. At 1 kHz in $\frac{1}{3}$-octave band, the modal density of the plate is 0·867 (modes/Hz) and the modal overlap factors are 8·7 and 86·7 for $\eta = 0{\cdot}01$ and 0·1 respectively. Statistically, about 200 modes exist within the $\frac{1}{3}$-octave band centered at 1 kHz. The value of α is 0·2614 (for $\eta = 0{\cdot}01$) or 2·614 (for $\eta = 0{\cdot}1$) at 1 kHz in $\frac{1}{3}$-octave band. From equation (50), the energy density integrated over $r_0 \leqslant r \leqslant 1$ is approximately 22·8% (for $\eta = 0{\cdot}01$) and 92·4% (for ($\eta = 0{\cdot}1$), respectively, as compared with that for $r_0 \leqslant r \leqslant \infty$ (range). Therefore, the latter case of $\eta = 0{\cdot}1$ can be considered as a highly damped case.

For the truncated analytical values, by using the modal summation technique, as many as 100×100 normal modes in sine functions were adopted. The band integration was performed for the third-octave band at the center frequency of 1 kHz after the frequency sweeping of nearly 1 Hz resolution. In applying RTM to the single plate, a total of 7204 ray tubes were employed and repeated calculations were carried out for each ray tube until

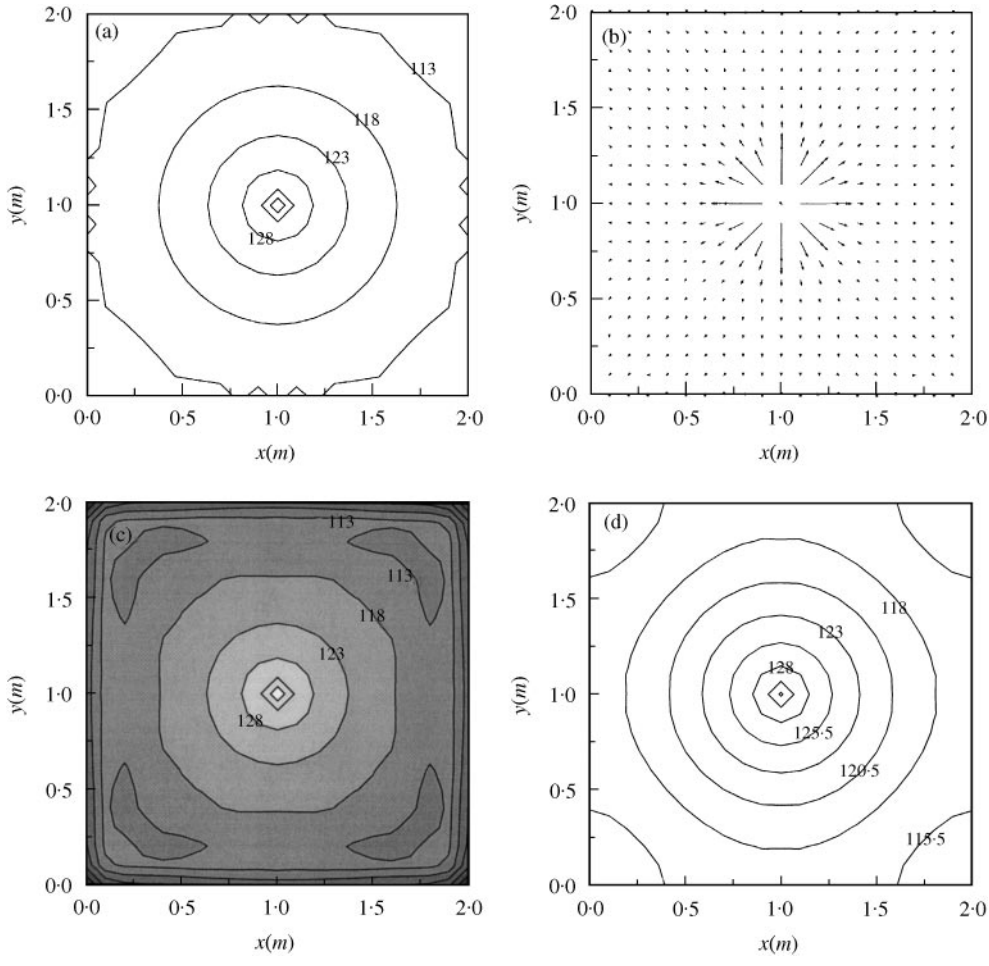

Figure 6. Predicted results for a single panel excited at the center point ($\eta = 0{\cdot}1, f_c = 1$ kHz in $\frac{1}{3}$-octave band). (a), (c), (d) Predicted distribution of vibration levels (dB re 1e-8 m/s); (b) intensity vectors. (a), (b) RTM; (c) mode summation method; (d) VCA. SEA result for this case is 120·6 dB.

reaching the propagation distance $r = -\log_e(10^{-3})/\alpha$ (m) for $\eta = 0{\cdot}01$ case and $r = -\log_e(10^{-5})/\alpha$ (m) for $\eta = 0{\cdot}1$ case. SEA calculations were obtained by multiplying the last term in equation (54) by $\Delta\omega_c$, and VCA calculations were performed as in reference [6].

Figures 5 and 6 show the calculated vibration distributions when $\eta = 0{\cdot}01$ and 0·1 and Figure 7 represents those along $y = 1$ m. In Figure 5, compared with VCA result, RTM prediction for $\eta = 0{\cdot}01$ is seen to be more closer to the analytic result by using the modal summation method. VCA predicts nearly uniform level distribution of about 130 dB over the whole plate, while the analytical result near the excitation position is 139 dB or more. In addition, the level distribution by modal summation method has a decaying trend from the excitation point to boundaries and the vibration level becomes down to 127 dB near the boundary. Compared with the analytical result, the prediction by the proposed RTM shows a similar level distribution near the driving point and the level becomes nearly 129 dB by approaching the boundaries. Note that SEA result for this case is 130·6 dB. When $\eta = 0{\cdot}1$, the plate is now highly damped and the RTM prediction is very close to the analytic one nearly in the entire plate as illustrated in Figure 6. In contrast, VCA underestimates the

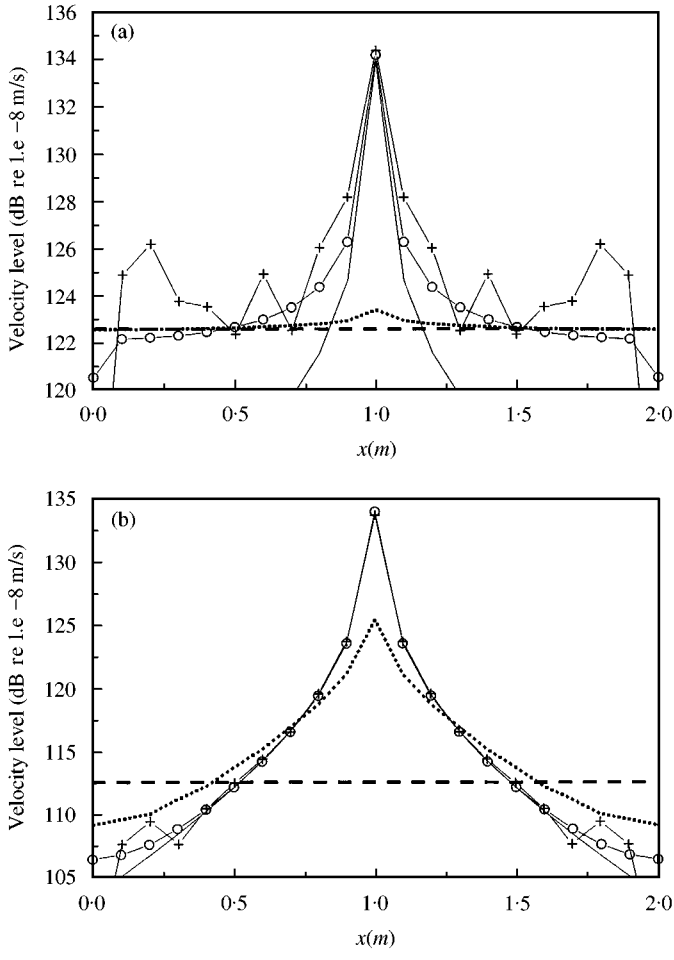

Figure 7. Comparison of predicted vibration levels along $y = 1$ m line: (a) $\eta = 0{\cdot}01$; (b) $\eta = 0{\cdot}1$: —+—, analytic; ·····, VCA; —○—, RTM; – – –, SEA; ——, infinite plate.

vibration level near the source position and overestimates near the boundaries. Note that SEA result for this case is 120·6 dB. The aforementioned features of prediction precision of RTM and VCA are illustrated more clearly in Figure 7. Again, one can confirm that RTM is superior to VCA in the estimation of the excitation level and the overall distribution of the vibration level, in particular for the highly damped panel. In Figure 7, an abrupt change of the predicted curves by RTM can be observed near the boundary and this is due to the limitation in the computing algorithm used here. Two small shaded regions near the boundaries can be seen in Figure 4, at which the propagation distance of each corresponding observation point is shorter than the starting distance r_1 or longer than the ending distance r_2. For simplicity, the calculations at the observation points within these regions were omitted and this is the cause of the abrupt changes in the predicted curve.

Figure 8 shows the comparisons of the predicted vibration levels with a frequency at an observation position. For the case of $\eta = 0{\cdot}01$, RTM shows little difference with SEA and VCA, and all methods are in good agreement with the analytic data, which shows a diminishing fluctuations with the frequency increase. However, when $\eta = 0{\cdot}1$, with increased frequency and compared with the spectral mean analytic results, predictions of SEA shows a large deviation and VCA overpredicts, but the prediction by RTM is in good

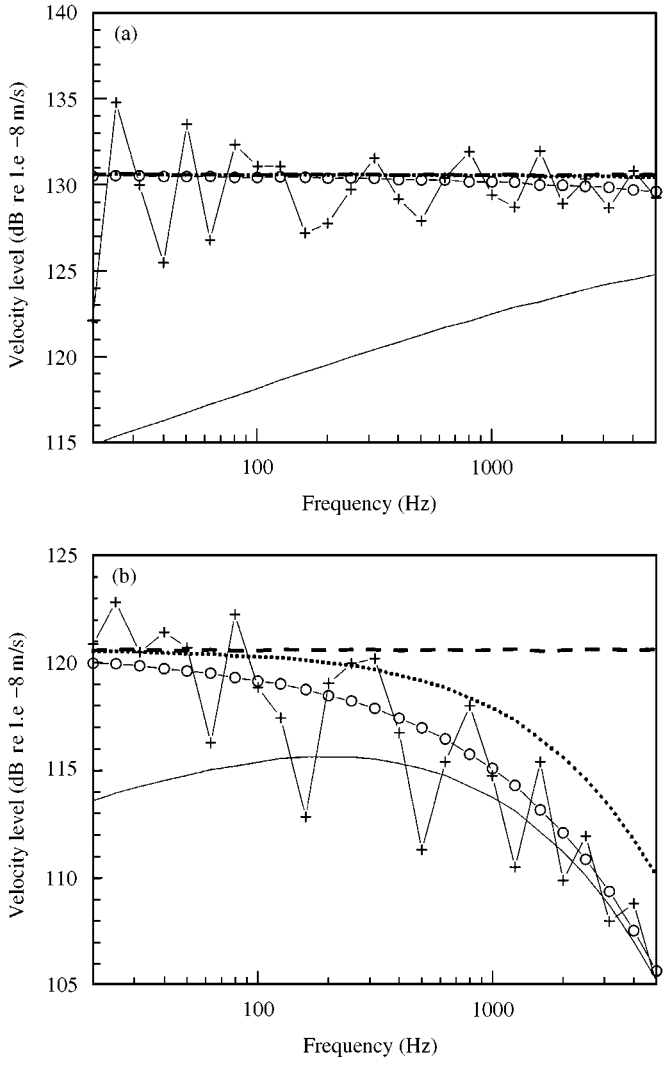

Figure 8. Comparison of predicted vibration levels with $\frac{1}{3}$-octave band analysis at $(x, y) = (1{\cdot}21, 1{\cdot}83)$ position: (a) $\eta = 0{\cdot}01$; (b) $\eta = 0{\cdot}1$: —+—, analytic; ·····, VCA; —○—, RTM; – – -, SEA; ——, infinite plate.

agreement. One can observe that RTM predictions are closing with the solution of infinite plate with an increased frequency and increased damping. The difference between RTM and the solution of infinite plate can be explained by the strength of the reverberant wave field. Comparisons of predicted total plate energy $\langle e_b \rangle$ with varying frequency are plotted in Figure 9. Predicted curves by all methods are nearly the same and in good agreement with the mean value of analytic results. As shown in Figure 9(b), it is interesting that SEA and VCA predict the analytic total plate energy very well although the plate is not in the non-reverberant condition.

3.2. TWO LINE-COUPLED PLATES

A structure composed of two identical square plates is chosen as a test model for the coupled structure. Two plated are joined at one common boundary and the material

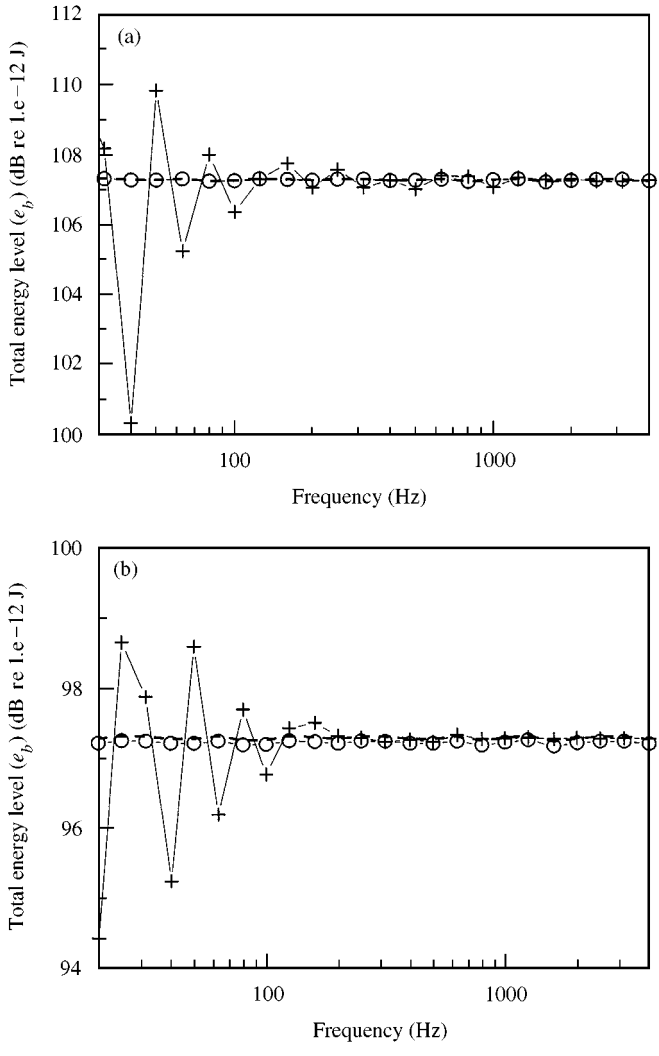

Figure 9. Comparison of predicted total energy of the plate with $\frac{1}{3}$-octave band analysis: (a) $\eta = 0{\cdot}01$; (b) $\eta = 0{\cdot}1$: —+—, analytic; —○—, RTM; – – – –, SEA, VCA.

properties and dimensions of each plate are the same as in the previous section. All boundaries of each plate are simply supported including the coupling boundary as shown in Figure 10. Plate 1 is driven by an excitation force 1 N at the center point.

Power transmission coefficient, $\tau(\phi) = \tau_0 \cos^2 \phi$, was taken from reference [27], where τ_0 denotes the power transmission coefficient for normal incident plane waves. In this case, $\tau_0 = 0{\cdot}5$ was used. Analytical data were obtained by using the modal summation method that has taken 500×500 modes into account for each plate by adopting sine functions in x and y directions [36]. Then, the band integration was performed with 1 Hz resolution in a frequency sweeping. VCA solutions for two line-coupled square plates were obtained using the procedure described in Appendix A. In applying RTM to the coupled plates, the same number of ray tubes with the single-plate case in the previous section was employed. Calculations were continued for each ray tube until reaching the propagation distance $r = -\log_e (10^{-3})/\alpha_1$ for $\eta = 0{\cdot}01$ case and $r = -\log_e (10^{-5})/\alpha_1$ for $\eta = 0{\cdot}1$ case, where

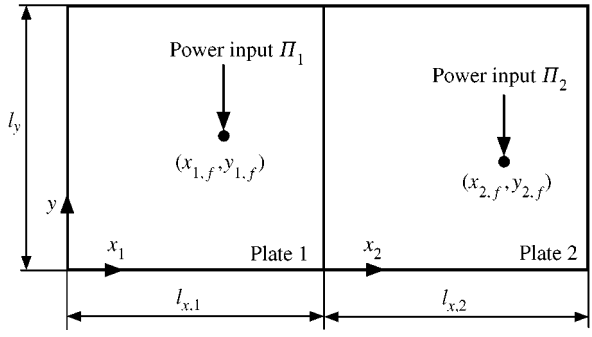

Figure 10. Schematic of the coupled square plates sharing a common line boundary.

α_1 equals the factor α in plate 1. SEA calculation were carried out with simple power balance equations [1, 16] with $\eta_{ij} = c_{g,i} l_y \langle \tau_{ij}(\phi) \rangle / \omega \pi S_i$, in which η_{ij} is the coupling loss factor from the ith to jth plate, l_y is the coupling length, S_i is the area of the ith plate, and $\langle \tau_{ij}(\phi) \rangle$ is the angle-averaged power transmission coefficient from the ith to the jth plate. Here, $2\tau(0)/3$ was adopted as $\langle \tau_{ij}(\phi) \rangle$ [27].

When the system is not very heavily damped ($\eta = 0{\cdot}01$), the velocity level distribution in plate 1 predicted by RTM is very close to the modal solution than that by VCA as can be seen in Figure 11. The whole predicted shape and condition are very similar to those of the single plate in the previous section. SEA result for this case is 129·9 dB. In Figure 12(a), except the data scatter within ± 1 dB, very good agreement can be observed between analytical and RTM results and the peaks and troughs are due to the strong modal behavior. In plate 2, VCA predicts nearly uniform level distribution along $y = 1$ m line while RTM result shows at least a slight decreasing trend. The differences between RTM or VCA and analytic calculation along this centreline could be ascribed to the local undulations in modal responses. This is due to the lack of damping and most of the areas in panel 2 have very similar levels to RTM or VCA result except local peaks. SEA result for this case is 122·2 dB. The integrated value of analytic results on plate 2 is 123·2 dB and both results of VCA and RTM are consistent with analytic values. However, compared with VCA result, the decreasing trend of RTM estimation is more alike with that of the analytic result near the joint and at the central region on plate 2 as can be seen in Figure 11(d). These features can be illustrated more clearly when the vibration levels are plotted along $y = 0{\cdot}7$ m line as shown in Figure 12(b).

Under the heavily damped condition of $\eta = 0{\cdot}1$, the overall characteristics obtained by various methods for plate 1 are almost identical to those of the single plate excitation in the previous section. That is, the RTM prediction closely approximates the analytic one nearly all over the plate as illustrated in Figure 13. In contrast, VCA underestimates the vibration level near the loading position and overestimates near the boundaries. Note that SEA result for this case is 120·5 dB. The aforementioned features of prediction precision of RTM and VCA are illustrated more clearly in Figure 14. In plate 2, one can find that both RTM and VCA yield very similar results to the analytic one, but the trend of RTM looks more closer to the analytically obtained vibration distribution. SEA result for this case is 103·5 dB.

As an additional example, two line-coupled plates with different lengths and thicknesses were considered. Plates 1 and 2 had a common length, l_y, of 1 m, and had length of x directional lengths 0·7 m ($l_{x,1}$) and 1·2 m ($l_{x,2}$) respectively. Their thickness were 3 and 4 mm respectively. Other material properties were the same with previous test plates. An angle-dependent power transmission coefficients were adopted from references [16, 27] and

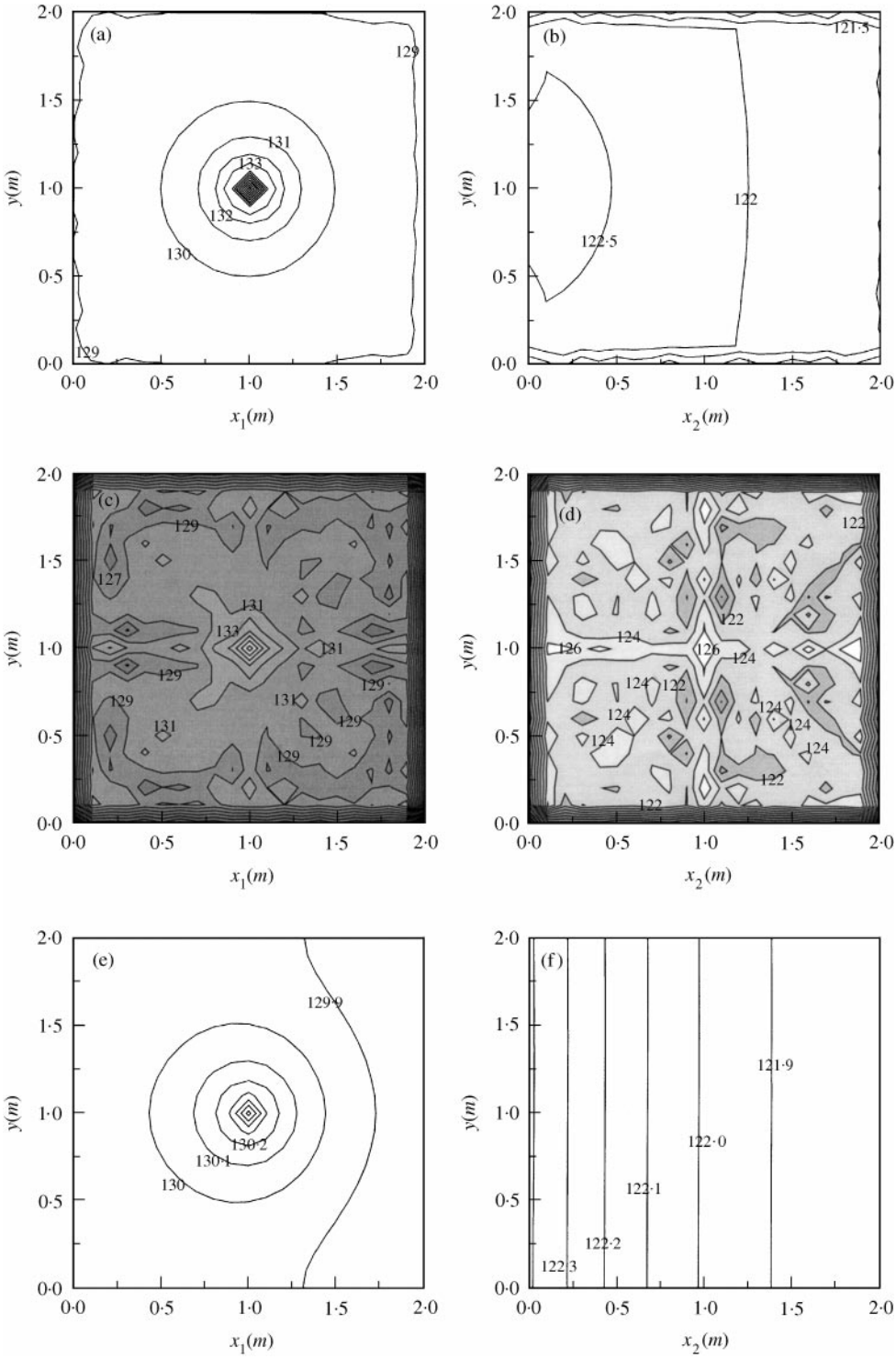

Figure 11. Predicted vibration level distribution for two coupled panels excited at the center point of panel 1 ($\eta = 0{\cdot}01$, $f_c = 1$ kHz in $\frac{1}{3}$-octave band). (a), (b) RTM; (c), (d) mode summation; (e), (f) VCA. (a), (c), (e) Plate 1; (b), (d), (f) plate 2. Predicted result by SEA is 129·9 dB for plate 1 and 122·2 dB for plate 2.

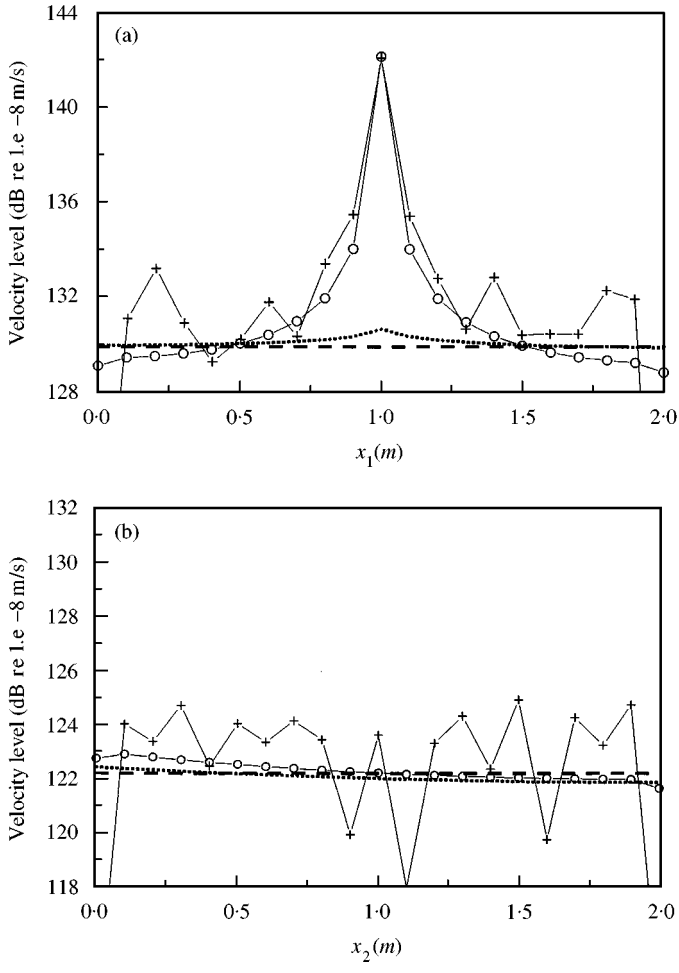

Figure 12. Comparison of predicted vibration levels for $\eta = 0{\cdot}01$; (a) plate 1 along $y = 1$ m; (b) plate 2 along $y = 0{\cdot}7$ m: —+—, analytic; ·····, VCA; —○—, RTM; – – –, SEA.

their angle-averaged values were used in applying SEA and VCA. Similar results but clearly showing the superiority of RTM were observed as illustrated in Figure 15.

3.3. A CONNECTED PANEL ARRAY

The vibration transmission characteristics were investigated for a four-panel array [16] as depicted in Figure 16. Four rectangular panels are connected in series and eight points of panel 1 are excited simultaneously. The longitudinal edges of the row are simply supported while the extreme transverse edges are fixed. All panels have the same loss factor $\eta = 0{\cdot}01$.

The same eight point-load locations were used as in reference [16] and the predicted values of exact analysis and WIA were also excerpted from there. It was said that the exact result, i.e., the result of the truncated modal summation, was given by the averages taken over the eight point-load locations. In calculating the VCA result, the same method as in the previous section was used. At the coupled boundaries, the power transmission coefficients function suggested in references [16, 27] were used in implementing the proposed RTM.

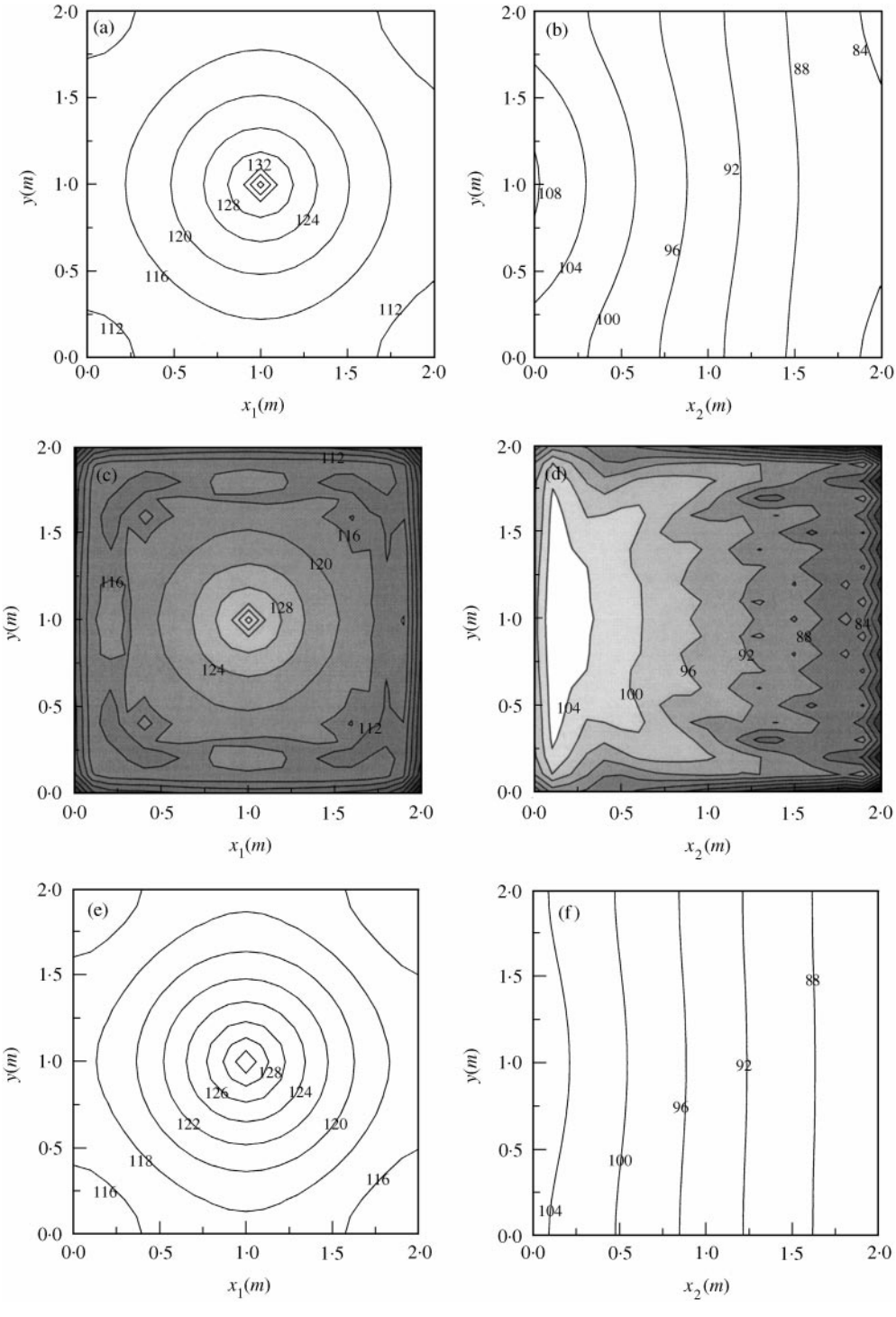

Figure 13. Predicted vibration level distribution for the two coupled panels excited at the center point of panel 1 ($\eta = 0{\cdot}1$, $f_c = 1$ kHz in 1/3-octave band). (a),(b) RTM; (c),(d) mode summation; (e),(f) VCA. (a),(c),(e) Plate 1; (b),(d),(f) plate 2. Predicted result by SEA is 120·5 dB for plate 1 and 103·5 dB for plate 2.

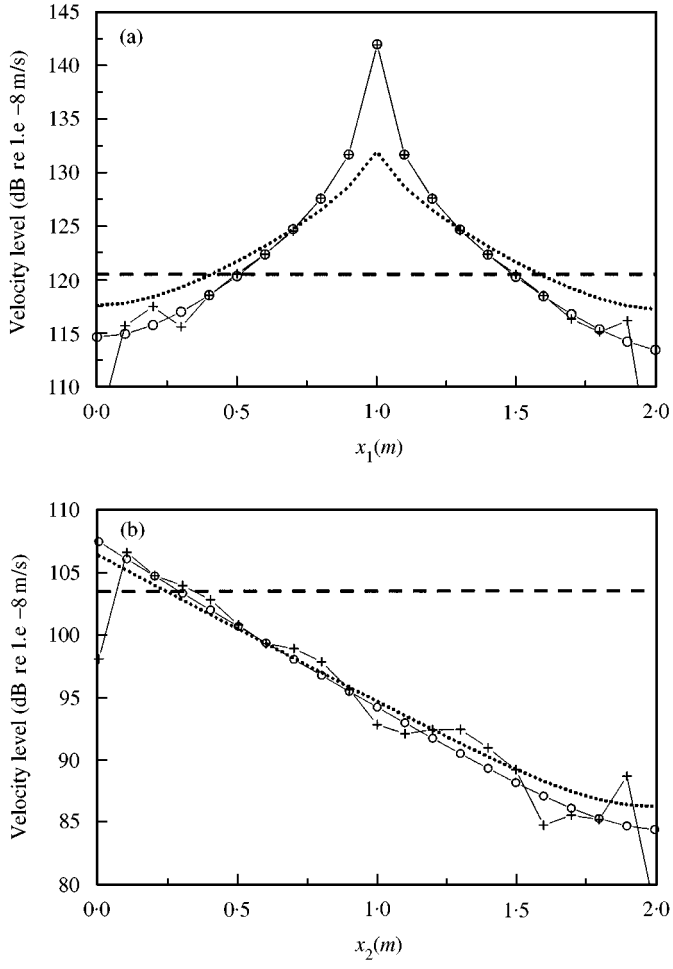

Figure 14. Comparison of predicted vibration levels for $\eta = 0{\cdot}1$: (a) plate 1 along $y = 1$ m; (b) plate 2 along $y = 0{\cdot}7$ m: —+—, analytic; ·····, VCA; —○—, RTM; – – –, SEA.

Additionally, in applying RTM to this panel array, the same calculation procedure was used as in the preceding section.

Results for the four-panel array are plotted in Figure 17. By comparing the energy ratio of plate 2 to plate 1, one can find that SEA over-predicts the vibration energy transmission by 2–4 dB and a similar result is obtained by VCA. In contrast, both WIA and RTM yield a similar trend of energy ratio spectrum to the analytic prediction, although the analytical result is scattered around WIA or RTM values. For energy ratio of plate 3 to plate 1, both SEA and VCA results again look slightly underestimating the vibration transmission and their slopes in spectra are different from the analytical one. They predict the lower vibration transmission at high frequencies than the analytical result. In contrast, RTM result is very consistent with the mean trend of the analytic one, whereas WIA slightly overpredicts the vibration transmission, in particular at low-frequency bands. A similar spectral slope can be observed for SEA and VCA. In Figure 17(c), the accuracy of various calculation methods is compared with the viewpoint of the energy transmission to the farthest panel from the driving panel. One can easily observe that the energy ratio of plate 4 to plate 1 is very much

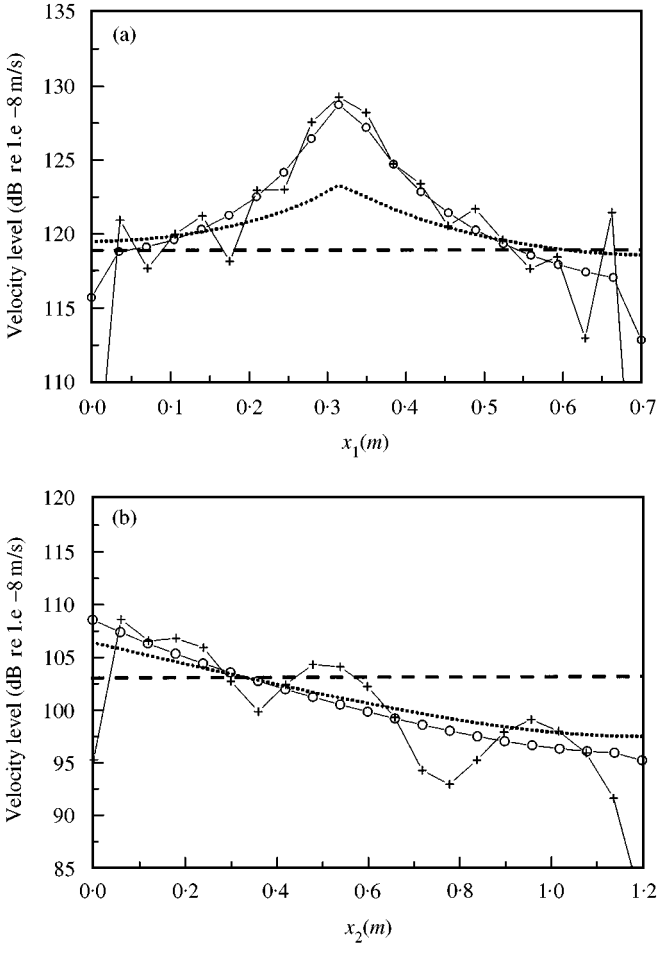

Figure 15. Comparison of predicted vibration levels for $\eta = 0{\cdot}1$ at 2 kHz $\frac{1}{3}$-octave band with a point force acting at (0·32, 0·43) of (a) plate 1 along $y = 0{\cdot}4$ m; (b) plate 2 along $y = 0{\cdot}4$ m: —+—, analytic; ·····, VCA; —○—, RTM; – – –, SEA.

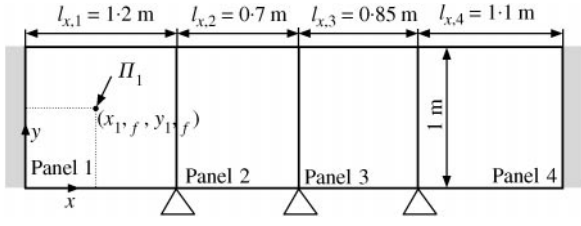

Figure 16. A four-panel array connected in series and excited at panel 1 at multiple points. The longitudinal edges of the row are simply supported while the extreme transverse edges (width = 1 m) are fixed. Thickness of plates 1, 2, 3, 4 are 4, 3, 4, 3 mm in their successive order respectively.

underestimated by SEA. However, results by both WIA and RTM agree reasonably with analytic energy ratio although the spectral shape of the energy ratio is different from each other. It is observed that the slope of the WIA result with the increasing frequency which is slightly steeper than that of the RTM.

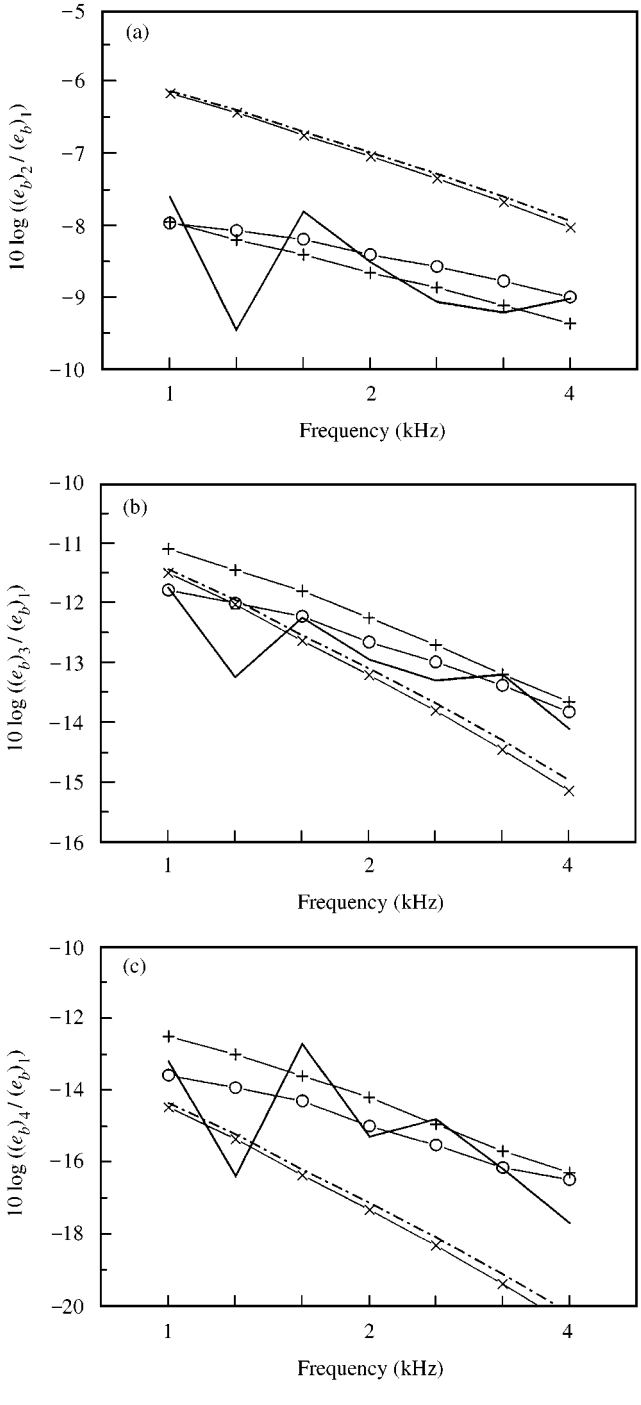

Figure 17. Comparison of calculated vibration energy vibration energy transmission for a four-panel array when the panel 1 is excited ($\eta = 0{\cdot}01$ for all panels). (a) $\langle e_b \rangle_2 / \langle e_b \rangle_1$, (b) $\langle e_b \rangle_3 / \langle e_b \rangle_1$, (c) $\langle e_b \rangle_4 / \langle e_b \rangle_1$: ——, analytic; –·–·–, SEA; —+—, WIA; —○—, RTM; —×—, VCA.

4. CONCLUDING REMARKS

In the paper, it has been shown that the proposed ray tracing method could be very useful in predicting the spatial distribution of vibration energy or velocity level of thin plates in good accuracy. The method is based on the concept of vibration field prediction taking into account of both direct and reverberant fields. Circular wave propagation diverging from the exciting position is considered and the direct field due to this is superposed with many ray tubes stemming from the multiple reflections from the boundaries. This feature permits the present method a capability to deal with the directional wave energy. Therefore, a quite refined accuracy in predicting the vibration energy can be attained for single or coupled thin plates at high frequencies compared with SEA or VCA techniques. Furthermore, RTM has superior features that the boundary shape can be taken into account and the wave filtering through the coupled boundary can also be analyzed. The present method has very similar characteristics to WIA in dealing with the directional wave energies. However, one can note that the proposed method can yield more improved result than WIA in predicting the spatial energy distribution, especially for the highly damped structure. It seems that the present method can deal with the inhomogeneous joint properties such as non-uniform reflection or transmission coefficient in the coupling boundaries. The specular reflections from the boundaries are only considered in this paper, but the scattering and diffraction effects may be included in the further study. Even though simple models such as the single plate and array plate were analyzed by the proposed RTM and the bending waves are only included in this article, box-like plate structures would be tackled with taking both bending and in-plane waves into account. Therefore, it is thought that the proposed ray tracing method can be one of the potentially useful tools in the power flow analysis of the vibrating structures at high frequencies.

REFERENCES

1. R. H. LYON 1975 *Statistical Energy Analysis of Dynamical Systems*: *Theory and Applications*. Cambridge: MIT Press.
2. D. J. NEFSKE and S. H. SUNG 1989 *Transactions of ASME*, *Journal of Vibration*, *Acoustics*, *Stress*, *and Reliability in Design* **111**, 94–100. Power flow finite element analysis of dynamic systems: basic theory and application to beams.
3. J. C. WOHLEVER and R. J. BERNHARD 1992 *Journal of Sound and Vibration* **153**, 1–19. Mechanical energy flow models of rods and beams.
4. O. M. BOUTHIER and R. J. BERNHARD 1992 *American Institute of Aeronautics and Astronautics Journal* **30**, 616–623. Models of space-averaged energetics of plates.
5. O. M. BOUTHIER and R. J. BERNHARD 1995 *Journal of Sound and Vibration* **182**, 129–147. Simple models of energy flow in vibrating membranes.
6. O. M. BOUTHIER and R. J. BERNHARD 1995 *Journal of Sound and Vibration* **182**, 149–164. Simple models of the energetics of transversely vibrating plates.
7. R. S. LANGLEY 1991 *Journal of Sound and Vibration* **150**, 47–65. Analysis of beam and plate vibrations by using the wave equation.
8. R. S. LANGLEY 1995 *Journal of Sound and Vibration* **182**, 637–657. On the vibrational conductivity approach to high frequency dynamics for two-dimensional structural components.
9. H. S. KIM, H. J. KANG, and J. S. KIM 1994 *Journal of Sound and Vibration* **174**, 493–504. A vibrational analysis at high frequencies by the power flow method.
10. A. CARCATERRA and A. SESTIERI 1995 *Journal of Sound and Vibration* **188**, 269–282. Energy density equations and power flow in structures.
11. A. CARCATERRA and A. SESTIERI 1995 *Journal of Sound and Vibration* **188**, 283–295. An envelope energy model for high frequency dynamic structures.
12. A. CARCATERRA and A. SESTIERI 1995 *Journal of Sound and Vibration* **201**, 205–233. Complex envelope displacement analysis: a quasi-static approach to vibrations.
13. M. J. SMITH 1995 *Journal of Sound and Vibration* **202**, 375–394. A hybrid energy method for predicting high frequency vibrational response of point-loaded plates.

14. A. LE BOT 1998 *Journal of Sound and Vibration* **211**, 537–554. A vibroacoustic model for high frequency analysis.
15. A. LE BOT 1998 *Journal of Sound and Vibration* **212**, 637–647. Geometric diffusion of vibrational energy and comparison with the vibrational conductivity approach.
16. R. S. LANGLEY 1992 *Journal of Sound and Vibration* **159**, 483–502. A wave intensity technique for the analysis of high frequency vibrations.
17. R. S. LANGLEY and A. N. BERCIN 1994 *Philosophical Transactions of Royal Society of London* A **346**, 489–499. Wave intensity analysis of high frequency vibrations.
18. M. R. SCHROEDER 1969 *Journal of the Acoustical Society of America* **47**, 424–431. Digital simulation of sound transmission in reverberant spaces.
19. M. R. SCHROEDER 1973 *American Journal of Physics* **41**, 461–471. Computer models for concert hall acoustics.
20. A. KROKSTAD, S. STROM and S. SORSDAL 1968 *Journal of Sound and Vibration* **8**, 118–125. Calculating the acoustical room response by the use of a ray tracing technique.
21. A. KULOWSKI 1982 *Applied Acoustics* **15**, 3–10. Relationship between impulse response and other types of room acoustical responses.
22. D. V. MAERCKE and J. MARTIN 1993 *Applied Acoustics* **38**, 93–114. The prediction of echograms and impulse responses within the Epidaure software.
23. T. LEWERS 1993 *Applied Acoustics* **38**, 161–178. A combined beam tracing and radiant exchange computer model of room acoustics.
24. M. VORLÄNDER 1989 *Journal of the Acoustical Society of America* **86**, 172–178. Simulation of the transient and steady-states sound propagation in rooms using a new combined ray-tracing/image-source algorithm.
25. E. DE GEEST and H. PATZOLD 1996 *Proceedings of inter-noise* **96**, 3177–3180. Comparison between room transmission functions calculated with arbitrary element method and a ray tracing method including phase.
26. H.-C. SHIN and J.-G. IH 1998 *Journal of the Acoustical Society of Korea* **17**, 54–61. Acoustic analysis of interior spaces by using the phased geometric acoustic model (in Korean).
27. L. CREMER, M. HECKL and E. E. UNGAR 1988 *Structure-Borne Sound*. Berlin: Springer, second edition.
28. E. SKUDRZYK 1980 *Journal of the Acoustical Society of America* **67**, 1105–1135. The mean-value method of predicting the dynamic response of complex vibrations.
29. R. GUNDA, S. M. VIJAYAKAR and R. SINGH 1995 *Journal of Sound and Vibration* **185**, 791–808. Method of images for the harmonic response of beams and rectangular plates.
30. J.-M. PAROT, CH THIRARD 1995 *Proceedings of Euro-Noise* **95**, 453–456. Ray techniques for modeling vibratory fields.
31. C. T. HUGIN 1997 *Journal of Sound and Vibration* **203**, 563–580. A physical description of the response of coupled beams.
32. G. PAVIC 1976 *Journal of Sound and Vibration* **49**, 221–230. Measurements of structure borne wave intensity. Part 1: formulation of the methods.
33. C. R. HALKYARD and B. R. MACE 1997 *Journal of Sound and Vibration* **203**, 101–126. A Fourier series approach to the measurement of flexural wave intensity in plates.
34. R. GUNDA, S. M. VIJAYAKAR and R. SINGH 1997 *Journal of the Acoustical Society of America* **102**, 326–334. Flexural vibration of an infinite wedge.
35. R. GUNDA, S. M. VIJAYAKAR, R. SINGH and J. E. FARSTAD 1998 *Journal of the Acoustical Society of America* **103**, 888–899. Harmonic Green's functions of a semi-infinite plate with clamped or free edges.
36. H. S. KIM, H. J. KANG and J. S. KIM 1994 *Journal of the Acoustical Society of America* **96**, 1557–1562. Transmission of bending waves in inter-connected rectangular plates.

APPENDIX A: A SOLUTION OF VIBRATION CONDUCTION EQUATION FOR TWO LINE-COUPLED SQUARE PLATES

Consider two square thin plates that are excited at points $(x_{1,f}, y_{1,f})$ and $(x_{2,f}, y_{2,f})$, respectively, and joined at an edge forming a line coupling as depicted in Figure 10. The

governing equations for vibration conduction analysis are given by [8]

$$-\frac{c_{g,j}^2}{\eta_i\omega}\left(\frac{\partial^2}{\partial x_i^2}+\frac{\partial^2}{\partial y^2}\right)e_i+\eta_i\omega e_i=\Pi_i\delta(x_i-x_{i,f},\,y-y_{i,f})\quad(i=1,2).\tag{A1}$$

From the conservation of net power flux [8], the boundary conditions for energy densities e_1 and e_2 can be expressed as follows:

$$-\frac{c_{g,j}^2}{\eta_i\omega}\nabla e_i\cdot\mathbf{n}_i\Big|_{y=0}=0,\quad-\frac{c_{g,j}^2}{\eta_i\omega}\nabla e_i\cdot\mathbf{n}_i\Big|_{y=l_y}=0\quad(i=1,2),\tag{A2a, A2b}$$

$$-\frac{c_{g,1}^2}{\eta_1\omega}\nabla e_1\cdot\mathbf{n}_1\Big|_{x_1=0}=0,\quad-\frac{c_{g,2}^2}{\eta_2\omega}\nabla e_2\cdot\mathbf{n}_2\Big|_{x_2=l_{x,2}}=0,\tag{A2c, A2d}$$

$$-\frac{c_{g,1}^2}{\eta_1\omega}\nabla e_1\cdot\mathbf{n}_1\Big|_{x_1=l_{x,1}}=\frac{\omega}{l_y}(S_1\eta_{12}e_1-S_2\eta_{21}e_2),\tag{A2e}$$

$$-\frac{c_{g,2}^2}{\eta_2\omega}\nabla e_2\cdot\mathbf{n}_1\Big|_{x_2=0}=\frac{\omega}{l_y}(S_1\eta_{12}e_1-S_2\eta_{21}e_2).\tag{A2f}$$

Here, $\mathbf{n}_i$ denotes the normal vector pointing outward from the ith boundary of the plate.

The following assumed solutions could be used by employing the eigenfunctions in the y direction that satisfies the boundary conditions of equations (A2a, b):

$$e_i=\sum_{m=0}^{\infty}F_{m,i}(x_i)\cos(m\pi y/l_y)\quad(i=1,2).\tag{A3}$$

Substituting these assumed solutions into equations (A1) and using the orthogonality property of eigenfunctions, the governing equations can be transformed into the following equations with index m:

$$-F''_{m,i}(x_i)+\beta_{m,i}^2F_{m,i}(x_i)=\Pi_i\delta(x_i-x_{i,f})\cos(m\pi y_{i,f}/l_y)/C_m/(c_{g,i}^2/\eta_i\omega)\quad(i=1,2).\tag{A4}$$

Here, the coefficients have the following meaning:

$$\beta_{m,i}^2=\left(\eta_i\omega+\frac{c_{g,i}^2}{\eta_i\omega}\left(\frac{m\pi}{l_y}\right)^2\right)\Big/\left(\frac{c_{g,i}^2}{\eta_i\omega}\right)\quad(i=1,2),\quad C_m=\int_0^{l_y}\cos^2(m\pi y/l_y)\,\mathrm{d}y.\tag{A5a, A5b}$$

Similarly, substituting the assumed solutions of equations (A3) into the boundary conditions of equations (A2c–f) and utilizing the orthogonality of eigenfunctions again, the boundary conditions can be transformed into the following equations with index m:

$$F'_{m,1}(x_1)=0\quad\text{at } x_1=0,\qquad F'_{m,2}(x_2)=0\quad\text{at } x_2=l_{x,2},\tag{A6a, b}$$

$$-\frac{c_{g,1}^2}{\eta_1\omega}\,F'_{m,1}\Big|_{x_1=l_{x,1}}=\frac{\omega}{l_y}(S_1\eta_{12}F_{m,1}|_{x_1=l_{x,1}}-S_2\eta_{21}F_{m,2}|_{x_2=0}),\tag{A6c}$$

$$-\frac{c_{g,2}^2}{\eta_2\omega}\,F'_{m,2}\Big|_{x_2=0}=\frac{\omega}{l_y}(S_1\eta_{12}F_{m,1}|_{x_1=l_{x,1}}-S_2\eta_{21}F_{m,2}|_{x_2=0}).\tag{A6d}$$

Provided that the plate 1 is driven at a point, solutions of equations (A4) can be assumed as follows:

$$F_{m,1}(x_1) = A_{m,1-}\exp(-\beta_{m,1}x_1) + B_{m,1-}\exp(\beta_{m,1}x_1) \quad \text{for } x_1 < x_{1,f}, \tag{A7a}$$

$$F_{m,1}(x_1) = A_{m,1+}\exp(-\beta_{m,1}x_1) + B_{m,1+}\exp(\beta_{m,1}x_1) \quad \text{for } x_1 < x_{1,f}, \tag{A7b}$$

$$F_{m,2}(x_1) = A_{m,2}\exp(-\beta_{m,2}x_2) + B_{m,2}\exp(\beta_{m,2}x_2). \tag{A7c}$$

When the conditions of source boundary, energy continuity and power injection are introduced into equations (A7), one can obtain

$$F_{m,1}(x_{1,f} - \Delta x/2) = F_{m,1}(x_{1,f} + \Delta x/2) \quad \text{as } \Delta x \to 0, \tag{A8a}$$

$$-F'_{m,1}\Big|_{x_{1,f}-\Delta x/2}^{x_{1,f}+\Delta x/2} = \Pi_1 \cos(m\pi y_{1,f}/l_y)/C_m/(c_{g,1}^2/\eta_1\omega) \quad \text{as } \Delta x \to 0. \tag{A8b}$$

Consequently, six unknown factors of $A_{m,1-}$, $B_{m,1-}$, $A_{m,1+}$, $B_{m,1+}$, $A_{m,2}$, and $B_{m,2}$ can be determined with the foregoing six boundary conditions. Equations (A7) can be obtained for each index m and, finally, the energy density at each plate can be calculated by substituting the obtained solutions into equations (A3).